THESIS FOR THE DEGREE OF MASTER OF SCIENCE

Prediction of the Axisymmetric Impinging Jet with Different $k - \varepsilon$ Turbulence Models

ALDO GERMÁN BENAVIDES MORÁN

Department of Thermo and Fluid Dynamics

CHALMERS UNIVERSITY OF TECHNOLOGY

Göteborg, Sweden 2004

Prediction of the Axisymmetric Impinging Jet with Different $k-\varepsilon$ Turbulence Models

ALDO GERMÁN BENAVIDES MORÁN

Diploma Work 04/29

Institutionen för termo- och fluiddynamik
Chalmers Tekniska Högskola
SE-412 96 Göteborg, Sweden
Phone +46-(0)31-7721400
Fax: +46-(0)31-180976

Printed at Chalmers Reproservice
Göteborg, Sweden 2004

Prediction of the Axisymmetric Impinging Jet with Different $k-\varepsilon$ Turbulence Models

by

Aldo Germán Benavides Morán
benavide@student.chalmers.se
Department of Thermo and Fluid Dynamics
Chalmers University of Technology
SE-412 96 Göteborg
Sweden

Abstract

The present work focuses on studying the axisymmetric turbulent impinging jet numerically. A low-Reynolds $k-\varepsilon$ model and the wall-normal Reynolds stress elliptic relaxation turbulence model ($\overline{v^2}-f$ model) are implemented in an in-house Navier-Stokes solver to accomplish the computations. In the present case, the inlet is located two diameters above the impingement wall; the Reynolds number is 2.3×10^4 and the flow being fully developed at the jet discharge. The different results are compared with existing experimental data for their validation.

The standard $k-\varepsilon$ model fails in predicting flow fields where a stagnation point is encountered and/or strong streamline curvature takes place. This is the case of the impinging flow which is dominated by irrotational straining and flow curvature. Due to its high heat transfer rates near the stagnation point, impinging jets have been used in many engineering and industrial applications where heating or cooling processes are required. Hence the necessity of developing improved turbulence models which let us correctly forecast the flow and thermal fields of this type.

The $\overline{v^2}-f$ model is found to perform much better than ordinary two-equation closure models for this flow configuration. As a consequence a new time scale constraint, based on the realizable $\overline{v^2}-f$ model, is implemented for the low-Reynolds $k-\varepsilon$ model. This time scale constraint substantially improves the flow predictions near the stagnation point and in the wall-jet region, as well as a better heat transfer coefficient is obtained. Finally, the use of a limiter for the production of kinetic energy in the low-Reynolds $k-\varepsilon$ model is also examined.

Acknowledgments

I would like to express my sincere thanks to Professor Lars Davidson, my supervisor, for his guidance and support throughout the course of this project. The many discussions I have had with him have benefitted considerably my understanding of *Computational Fluid Dynamics* (CFD) and turbulence modelling.

Understanding the code and clearing up the problems which sometimes came out was just not possible without the help and expertise of A. Sveningsson.

I have greatly enjoyed every single day of the last eighteen months studying in Chalmers and living in Sweden. I would like to thank everyone taking part in the Master's programme in Turbulence, specially to Professor W.K. George & Docent Gunnar Johansson for their constant support, advice and kindness no matter how busy they were. I have always been very proud of having the opportunity to participate in this extraordinary programme and I can say with no doubt it was one of the best experiences of my life, so far.

I specially thank my family for their support during my stay in Sweden. Without their help and encouragement nothing would have been possible.

Last, but by no means least, I would like to thank everyone at the Department, for making such a pleasant and work friendly atmosphere. Being part of TFD is wonderful!

Contents

Chapter 1

Introduction

The axisymmetric impinging jet studied in this work is a typical example of wall-bounded shear flows. The inlet flow which is fully developed exits a pipe of diameter D at a height of 2 jet diameters from the wall ($H/D = 2$), impinges onto the wall surface and disseminates radially along the solid boundary. Due to its high level of heat transfer rate near the stagnation point, jet impingement is used in many engineering and industrial applications where heating, cooling or drying processes are required. Examples of such applications are cooling of gas turbine blades and electronic equipment.

The flow field of an impinging jet comprises three distinctive flow regions, namely a free jet region, a deflection region (or stagnation region) and a wall jet region as shown in Figure 1.1. A shear layer is created due to the velocity difference between the potential core of the jet and the ambient fluid. Commonly this shear layer is the source of the turbulence in the jet, however as the inlet-to-wall distance is so short in the present case, there is not enough gap for mixing to happen with the surrounding fluid. As a result, the flow field in the vicinity of the stagnation point has a low turbulence intensity.

In the free jet region, the mean shear strain is zero and the production of kinetic energy is exclusively due to the normal straining. As the flow approaches the wall, the centerline velocity decreases to zero at the stagnation point. Moreover, the proximity of the solid boundary causes the deflection of the jet and a strong streamline curvature region is observed. Downstream the stagnation point, a wall jet evolves along the wall. Turbulence energy is increased due to the mean shear strain which dominates in the near-wall region.

1.1 Relevant past studies

All the flow characteristics described above make the axisymmetric impinging jet a challenging case for turbulence models. Previous numerical computations revealed the lack of accuracy of some models in pre-

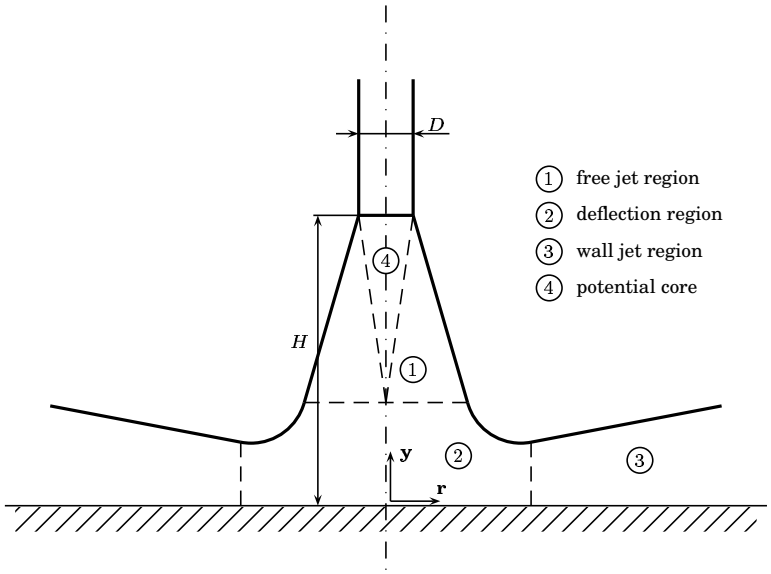

Figure 1.1: Flow regions of an axisymmetric impinging jet

dicting the turbulent quantities near the stagnation point. As an example, the standard $k-\varepsilon$ model overestimates the turbulent kinetic energy in the deflection region, leading to extremely high values of the computed heat transfer coefficient. Numerous computations with different configurations of impinging jets have been carried out, showing that the *RANS* (*Reynolds-Averaged Navier-Stokes equations*) models perform reasonably well in most of the flow domain. However, the stagnation and near-wall regions are not properly resolved by most eddy-viscosity models. Attempts to improve the eddy-viscosity assumption using new velocity and time scales in the definition of the turbulent viscosity show that the performance of two-equation models can be further enhanced [17]. Although *Reynolds Stress Models* (*RSM*) perform correctly in the presence of a stagnation point and to streamline curvature, their implementation is quite complicated. Also, *RSM* are computationally more demanding as an equation is solved for each Reynolds stress. A good compromise can be achieved with the wall-normal Reynolds stress elliptic relaxation model ($\overline{v^2}-f$ model) which solves a stress transport equation and an elliptic function to account for near-wall effects instead of using damping functions. Even so, it still employs the eddy viscosity assumption to close the equation system. It is reported [4] that the model has performed well in stagnation flows and near-wall turbulence.

1.2 Experimental test case for validation

The experimental case selected to validate the results of this work is a set of flow measurements carried out by *Cooper et al.* [5] and the heat transfer data of *Baughn et al.* [3] which have been widely used by researchers to test turbulence models. Hot-wire measurements have been carried out employing two different inlet pipe diameters, varying the inlet-to-plate distance from two to ten diameters and considering two Reynolds numbers (2.3×10^4 and 7×10^4).

Experimental data of mean velocity, normal stresses and turbulent shear stress are available at a number of radial locations. Heat transfer data are reported in the form of Nusselt number as a function of radial position r/D. For a detailed description of the experiment see the cited references as well as the ERCOFTAC database
http://ercoftac.mech.surrey.ac.uk

Only one set of experimental data has been used to validate the results of the present work, namely $Re_{\mathrm{D}} = 2.3 \times 10^4$ and $H/D = 2$.

Chapter 2

Governing Equations

All fluid motions (laminar or turbulent) are governed by a set of dynamical equations, namely the *Continuity equation* and the *Momentum equation*, which can be written in cartesian coordinates using tensor notation as

$$\left[\frac{\partial \tilde{\rho}}{\partial t} + \tilde{u}_j \frac{\partial \tilde{\rho}}{\partial x_j}\right] + \tilde{\rho}\frac{\partial \tilde{u}_j}{\partial x_j} = 0 \tag{2.1}$$

$$\tilde{\rho}\left[\frac{\partial \tilde{u}_i}{\partial t} + \tilde{u}_j \frac{\partial \tilde{u}_i}{\partial x_j}\right] = -\frac{\partial \tilde{p}}{\partial x_i} + \frac{\partial \tilde{T}_{ij}^{(v)}}{\partial x_j} \tag{2.2}$$

where $\tilde{u}_i(\vec{x},t)$, $\tilde{p}(\vec{x},t)$ and $\tilde{T}_{ij}(\vec{x},t)$ represent the i-th component of the fluid velocity, the static pressure and the viscous stress tensor, respectively, at a point in space $\vec{x}$ and time t. $\tilde{\rho}$ is the fluid density. Body forces are not taken into account and the tilde symbol indicates that an instantaneous quantity is being considered.

For many flows of interest, the fluid behaves as a Newtonian fluid in which the viscous stress tensor is related to the fluid motion using a property of fluid, the molecular viscosity (μ)

$$\tilde{T}_{ij}^{(v)} = 2\mu\left(\tilde{s}_{ij} - \frac{1}{3}\tilde{s}_{kk}\delta_{ij}\right) \tag{2.3}$$

$\tilde{s}_{ij}$ is the instantaneous strain-rate tensor given by

$$\tilde{s}_{ij} = \frac{1}{2}\left(\frac{\partial \tilde{u}_i}{\partial x_j} + \frac{\partial \tilde{u}_j}{\partial x_i}\right) \tag{2.4}$$

For incompressible flows, any derivative of density is zero and hence 2.1 & 2.2 are simplified to obtain the *Navier-Stokes equations*

$$\frac{\partial \tilde{u}_j}{\partial \tilde{x}_j} = 0 \tag{2.5}$$

$$\frac{\partial \tilde{u}_i}{\partial t} + \tilde{u}_j \frac{\partial \tilde{u}_i}{\partial x_j} = -\frac{1}{\rho}\frac{\partial \tilde{p}}{\partial x_i} + \nu\frac{\partial^2 \tilde{u}_i}{\partial x_j \partial x_j} \tag{2.6}$$

where constant kinematic viscosity ($\nu \equiv \mu/\rho$) is also assumed. Now, we have a system of four equations which form a complete description of the velocity and pressure fields. The system of equations can be solved numerically, without further assumptions, if appropriate boundary and initial conditions are established. However this is only possible for relatively low-Reynolds number flows. This procedure is known as *Direct Numerical Simulation* or *DNS*, which would require extremely high computer resources if all the scales of a turbulent flow are to be resolved. Therefore, it is unlikely that *DNS* will be generally used in industrial flow computations for the foreseeable future.

An alternative approach is to consider a turbulent flow as consisting of two components, a mean part and a fluctuating part

$$\begin{aligned} \tilde{u}_i &= U_i + u_i \\ \tilde{p} &= P + p \\ \tilde{s}_{ij} &= S_{ij} + s_{ij} \end{aligned}$$

This method of decomposing is referred to as *Reynolds Decomposition*. Introducing these decomposition into the instantaneous equations and *time-averaging* results in the *Reynolds Averaged Navier-Stokes* (*RANS*) equations.

$$\frac{\partial U_j}{\partial x_j} = 0 \tag{2.7}$$

$$U_j \frac{\partial U_i}{\partial x_j} = -\frac{1}{\rho}\frac{\partial P}{\partial x_i} + \frac{\partial}{\partial x_j}\left[\nu \frac{\partial U_i}{\partial x_j} - \overline{u_i u_j}\right] \tag{2.8}$$

These equations look very similar to the un-averaged *Navier-Stokes equations* (2.1 & 2.2) but for a new term which represents the correlation between fluctuating velocities, known as *Reynolds stress tensor*, $\overline{u_i u_j}$ (the overbar denotes *time-averaging*). This term encompasses all effects the turbulent motion has on the mean flow. On the other hand, the process of averaging adds six new independent unknowns ($\overline{u_i u_j}$ is a symmetric tensor) to the three mean velocity components and the mean pressure gradient. Thus, $\overline{u_i u_j}$ must be related to the mean motion itself if we want to close the equation system. This is referred to as the *closure problem of turbulence*.

As a result, the *Reynolds stress tensor* needs to be properly modeled if simulations of complex turbulent flows are to be performed at an attainable computational cost. The most important RANS models are the *Eddy-Viscosity Models* (*EVM*) and the *Reynolds Stress Transport Model* (*RSTM*) which will be briefly discussed later.

A detailed heat transfer analysis requires consideration of the *Energy equation*, which is further simplified for incompressible flow with constant properties and adding a relation for the heat conduction term

(Fourier's law)

$$\tilde{u}_j \frac{\partial \tilde{\theta}}{\partial x_j} = \frac{\nu}{Pr} \frac{\partial^2 \tilde{\theta}}{\partial x_j \partial x_j} \tag{2.9}$$

where $\tilde{\theta}$ is the instantaneous temperature, and Pr the Prandtl number of the fluid given by,

$$Pr = \frac{\mu C_p}{\kappa}$$

where C_p and κ are the specific heat and thermal conductivity respectively.

If we apply Reynolds decomposition ($\tilde{\theta} = \Theta + \theta$) to equation 2.9 followed by time-averaging, the result is a new *RANS* equation for the mean temperature

$$U_j \frac{\partial \Theta}{\partial x_j} = \frac{\partial}{\partial x_j} \left[\frac{\nu}{Pr} \frac{\partial \Theta}{\partial x_j} - \overline{u_j \theta} \right] \tag{2.10}$$

The last procedure added three new terms ($\overline{u_j \theta}$) known as the turbulent heat fluxes, which link the velocity and temperature fluctuations and need also to be modeled.

Eddy Viscosity Models

EVM employ a direct correspondence to the representation of the viscous stress tensor, as given in equation 2.3, to model the Reynolds stress tensor

$$-\overline{u_i u_j} = 2\,\nu_t S_{ij} - \frac{2}{3} k \delta_{ij} \tag{2.11}$$

This is referred to as the *Boussinesq assumption*, which relates the Reynolds stress tensor and the mean velocity gradients (S_{ij} is the mean strain-rate and k the turbulent kinetic energy per unit mass) by means of a scalar quantity ν_t known as the *turbulent viscosity* or *eddy-viscosity*. Based on dimensional analysis, the eddy-viscosity is commonly defined as the product of a turbulent velocity scale ($\mathcal{V}$) and a turbulent time scale ($\mathcal{T}$)

$$\nu_t = c_\mu \mathcal{V}^2 \mathcal{T} \tag{2.12}$$

where c_μ is a constant. There exist different types of *EVM* depending on the choice of these turbulent scales to close the eddy-viscosity. Besides, additional modeled transport equations are usually solved for the turbulent quantities.

Reynolds Stress Transport Models

The *RSTM* are a more sophisticated approach to the closure problem. Instead of modelling the Reynolds stresses, a (modeled) transport equation for each one is solved. However, *RSTM* are much more complex and

difficult to implement as additional unknown terms come out, which need to be modeled

$$U_k \frac{\partial \overline{u_i u_j}}{\partial x_k} = D_{ij} + \Phi_{ij} + P_{ij} - \varepsilon_{ij} \tag{2.13}$$

The terms on the right hand side of 2.13 are respectively, *diffusion* (D_{ij}, or turbulent transport term), *pressure-strain correlation* (Φ_{ij}, or redistribution term), *production* (P_{ij}) and *dissipation* (ε_{ij}). The production is the only term which does not require modelling as it is computed in its exact form. Contracting the free indices in 2.13 ($i = j$) and dividing by two, we get an equation for the turbulent kinetic energy ($k \equiv \frac{1}{2}\overline{u_i u_i}$)

$$U_j \frac{\partial k}{\partial x_j} = D_k + P_k - \varepsilon \tag{2.14}$$

where only the diffusion, the production and the rate of dissipation of kinetic energy (ε) terms are present. The latter term also plays an important role in deriving the time scale (equation 2.12) of some eddy-viscosity models. The exact production term in equation 2.14, which will be examined in the following chapters, is given by

$$P_k = -\overline{u_i u_j} \frac{\partial U_i}{\partial x_j} \tag{2.15}$$

P_k usually takes energy from the mean flow to increase the turbulence. It will be shown that appropriate modelling of P_k is essential for impinging jet flow predictions.

Chapter 3

Turbulence Models Considered

3.1 Low-Reynolds-Number $k-\varepsilon$ Model

The model of *Abe-Kondoh-Nagano* (*AKN model*) can accurately predict the near-wall limiting behavior in a variety of wall-bounded flows employing a couple of *damping functions*. The square root of the turbulent kinetic energy ($\sqrt{k}$) is used as the obvious velocity scale in equation 2.12, while the dissipation rate is used to form the time scale. The modeled k and ε equations are given below together with the respective wall-boundary conditions. For a complete description of the *AKN model* see reference [1].

$$U_j \frac{\partial k}{\partial x_j} = \frac{\partial}{\partial x_j}\left[\left(\nu + \frac{\nu_t}{\sigma_k}\right)\frac{\partial k}{\partial x_j}\right] + P_k - \varepsilon \tag{3.1}$$

$$U_j \frac{\partial \varepsilon}{\partial x_j} = \frac{\partial}{\partial x_j}\left[\left(\nu + \frac{\nu_t}{\sigma_\varepsilon}\right)\frac{\partial \varepsilon}{\partial x_j}\right] + \frac{1}{\mathcal{T}}\left(C_{\varepsilon 1} P_k - C_{\varepsilon 2} f_\varepsilon \varepsilon\right) \tag{3.2}$$

$$\mathcal{T} = \frac{k}{\varepsilon}$$

$$f_\varepsilon = \left[1 - \exp\left(-\frac{y^*}{3.1}\right)\right]^2 \left[1 - 0.3\,\exp\left\{-\left(\frac{R_t}{6.5}\right)^2\right\}\right]$$

$$y^* = y\left(\frac{\varepsilon}{\nu^3}\right)^{1/4}$$

$$R_t = \frac{k^2}{\nu\varepsilon}$$

where y is the distance from the wall, R_t is the turbulent Reynolds number and $\mathcal{T}$ the time scale needed to define the eddy-viscosity

$$\nu_t = C_\mu f_\mu k \mathcal{T} = C_\mu f_\mu \frac{k^2}{\varepsilon} \tag{3.3}$$

and f_μ the damping function to take into account the near-wall effects on ν_t

$$f_\mu = \left[1 - \exp\left(-\frac{y^*}{14}\right)\right]^2 \left[1 + \frac{5}{R_t^{3/4}} \exp\left\{-\left(\frac{R_t}{200}\right)^2\right\}\right]$$

The constants of the model are given in the following table:

$C_\mu = 0.09$	$C_{\varepsilon 1} = 1.5$	$C_{\varepsilon 2} = 1.9$	$\sigma_k = 1.4$	$\sigma_\varepsilon = 1.4$

The production term (equation 2.15) is computed using the Boussinesq assumption (2.11) as

$$P_k = 2\,\nu_t S^2 \tag{3.4}$$

where $S = \sqrt{S_{ij} S_{ij}} \geq 0$, is the mean strain-rate magnitude.

Wall Boundary Conditions

The turbulent kinetic energy goes to zero at the wall whereas ε retains a finite value on the wall surface according to the near wall limiting behavior

$$k_w = 0 \tag{3.5}$$

$$\varepsilon_w = 2\,\nu \frac{k_1}{y_1^2} \tag{3.6}$$

the indices w and 1 denote the wall and the nearest grid point from the wall, respectively. A complete derivation of the ε_w boundary condition is found in references [1] and [17].

3.2 Standard $\overline{v^2} - f$ Model

The $\overline{v^2} - f$ (or $V2F$) model does not use the damping functions of the previous section to solve the k and ε equations (setting $f_\varepsilon = 1$ on the right hand side of equation 3.2, we get the *standard* $k-\varepsilon$ model). Instead, a *wall-normal Reynolds stress* ($\overline{v^2}$) is introduced together with an elliptic relaxation function (f) which handles the wall damping effects on the stress component. Then, an additional modeled transport equation must be solved for the $\overline{v^2}$ stress, which is derived from the exact Reynolds stress transport equation, especially looking at the redistribution term in equation 2.13 to take into account the damping effects. A detailed description of the $\overline{v^2} - f$ model along with its derivation is found in references [12] and [16].

$$\frac{\partial \overline{v^2}}{\partial t} + U_j \frac{\partial \overline{v^2}}{\partial x_j} = \frac{\partial}{\partial x_j}\left[\left(\nu + \frac{\nu_t}{\sigma_k}\right)\frac{\partial \overline{v^2}}{\partial x_j}\right] + kf - 6\overline{v^2}\frac{\varepsilon}{k} \tag{3.7}$$

$$L^2 \frac{\partial^2 f}{\partial {x_j}^2} - f = \frac{C_1}{\mathcal{T}}\left(\frac{\overline{v^2}}{k} - \frac{2}{3}\right) - C_2\frac{P_k}{k} - \frac{1}{\mathcal{T}}\left(6\frac{\overline{v^2}}{k} - \frac{2}{3}\right) \tag{3.8}$$

The time ($\mathcal{T}$) and length (L) scales are given by

$$\mathcal{T} = \max\left(\frac{k}{\varepsilon}\ ,\ 6\sqrt{\frac{\nu}{\varepsilon}}\right) \tag{3.9}$$

$$L = C_L \max\left[\frac{k^{3/2}}{\varepsilon}\ ,\ C_\eta\left(\frac{\nu^3}{\varepsilon}\right)^{1/4}\right] \tag{3.10}$$

where the time-scale has been bounded such that it will not be smaller than the *Kolmogorov time-scale* ($\tau_K = \sqrt{\nu/\varepsilon}$). This limit guarantees to avoid singularities in the governing equations as the wall is approached. Making use of the new velocity scale ($\mathcal{V} = (\overline{v^2})^{1/2}$), the eddy-viscosity is defined as

$$\nu_t = C_\mu \overline{v^2}\mathcal{T} \tag{3.11}$$

The "constant" $C_{\varepsilon 1}$ (equation 3.2) is also damped near the wall according to

$$C_{\varepsilon 1} = 1.4\left(1 + C_{\varepsilon d}\sqrt{k/\overline{v^2}}\right) \tag{3.12}$$

and the remaining constants of the model are listed on the table below:

$C_\mu = 0.22$	$C_{\varepsilon d} = 0.050$	$C_{\varepsilon 2} = 1.9.$	$C_1 = 1.4$	$C_2 = 0.3$
$\sigma_k = 1.0$	$\sigma_\varepsilon = 1.3$	$C_L = 0.23$	$C_\eta = 70$	–

Wall Boundary Conditions

The k and ε wall boundary conditions are the same as the ones given by equations 3.5 and 3.6 in the *AKN model*. Besides, the wall-normal Reynolds stress and the relaxation function go to zero at the wall for the modeled equations considered here [16]

$$\overline{v_w^2} = 0 \tag{3.13}$$

$$f_w = 0 \tag{3.14}$$

3.3 Realizable $\overline{v^2}-f$ Model

The modeled production of kinetic energy (equation 3.4) becomes very large at the stagnation region due to the high value of the strain-rate magnitude, S. That is the reason why the turbulent kinetic energy is high at this point. On the other hand, it should be checked that all the normal stresses remain positive, say $\overline{u_i^2} \geq 0$. Durbin [13] imposed a time scale constraint for the $\overline{v^2}-f$ model based on this realizable criteria which is of great importance for *EVM* in stagnation flow. The Boussinesq assumption (equation 2.11) for the normal stress to the impingement wall (see Figure 1.1) can be simplified to

$$\overline{u_2^2} \;=\; \frac{2}{3}k - 2\,\nu_t S_{22} \tag{3.15}$$

If S_{22} gets too large, then $\overline{u_2^2} \leq 0$ which is unphysical. Thus, let's examine when S_{22} becomes largest. The symmetric strain-rate tensor S_{ij} has real eigenvalues and is diagonal in principal-axes coordinates. The diagonal elements of S_{ij} in the rotated coordinate system are its eigenvalues ($\lambda_\beta, \beta = 1, 2$) which can be found solving the equation

$$|S_{ij} - \lambda_\beta| \;=\; 0 \tag{3.16}$$

In two dimensions, the solution of 3.16 along with the incompressible flow assumption ($S_{11} + S_{22} = 0$, equation 2.7) gives

$$|\lambda_\beta| = \sqrt{\frac{1}{2}S_{ij}S_{ij}} = \sqrt{\frac{1}{2}S^2} \tag{3.17}$$

As all the strains are now normal, equation 3.15 results in (also imposing the realizability constraint)

$$\begin{aligned} \overline{u_\beta^2} \;&=\; \frac{2}{3}k - 2\,\nu_t|\lambda_\beta| \;\geq\; 0 \\ \nu_t \;&\leq\; \frac{k}{3|\lambda_\beta|} \end{aligned} \tag{3.18}$$

The equation above gives a bound on the eddy-viscosity. If the definition of ν_t for the $\overline{v^2}-f$ model is now used (equation 3.11) together with equation 3.17, the following constraint on the time scale $\mathcal{T}$ comes about

$$\mathcal{T} \leq \frac{\sqrt{2}}{3}\frac{k}{C_\mu \overline{v^2} S} \tag{3.19}$$

The derived constraint on $\mathcal{T}$ lowers its value, leading to a smaller eddy-viscosity which counteracts the high strain-rates. This is the way the production of kinetic energy is diminished in the stagnation region. Finally, equations 3.9 and 3.19 can be merged to fulfil all the turbulent

time scale demands (a model constant is also added on equation 3.19, see reference [16])

$$\mathcal{T} \;=\; \min\left[\max\left(\frac{k}{\varepsilon}\,,\; 6\sqrt{\frac{\nu}{\varepsilon}}\right)\;,\; \frac{0.6\,k}{\sqrt{6}\,C_\mu \overline{v^2} S}\right] \tag{3.20}$$

A similar realizable condition has been also proposed for the length scale L [16], and it reads

$$L \;=\; C_L\,\max\left\{\min\left[\frac{k^{3/2}}{\varepsilon}\;,\; \frac{k^{3/2}}{\sqrt{6}\,C_\mu \overline{v^2} S}\right]\;,\; C_\eta\left(\frac{\nu^3}{\varepsilon}\right)^{1/4}\right\} \tag{3.21}$$

Although it was implemented, it was found that the limitation on L is not as significant as that for T.

Implementing the Realizability Constraint for the $\overline{v^2} - f$ Model

Equation 3.8 is of elliptic character so that disturbances in one point propagate throughout the whole computational domain. Due to the intricate coupling between equations 3.7 and 3.8 along with the time scale limit of 3.20, the computations are likely to diverge if the realizability constraint is not implemented in a compatible manner. The main reason why a given simulation might diverge is directly related to the magnitude of f in the domain. If f gets too large, then the source term kf in equation 3.7 increases the production of the normal stress such that $\overline{v^2} \geq \frac{2}{3}k$ which also have a feedback on f [17]. To overcome this issue, the right hand side of 3.8 (its *source term*) can be used as an upper bound on f for the term kf in the $\overline{v^2}$ equation [9]

$$f_{source\;\overline{v^2}} = \min\left\{f\;,\; -\frac{1}{\mathcal{T}}\left[(C_1 - 6)\,\frac{\overline{v^2}}{k} - \frac{2}{3}\,(C_1 - 1)\right] + \frac{C_2 P_k}{k}\right\} \tag{3.22}$$

where $\mathcal{T}$ is the old time scale (equation 3.9) without the realizability condition for stagnation flow. Instead of explicitly using the constraint on $\mathcal{T}$ in equations 3.7 and 3.8, it is imposed for the ratio $\overline{v^2}/k$ as

$$\frac{\overline{v^2}}{k} \;=\; \min\left(\frac{\overline{v^2}}{k}\;,\; \frac{0.6}{\sqrt{6}\,C_\mu \mathcal{T} S}\;,\; 2\right) \tag{3.23}$$

This limit is only used in the f and $\overline{v^2}$ equations together with the old time scale given in equation 3.9. For the k and ε equations the new time scale limit is turned on (equation 3.20) as well as for the definition of the eddy-viscosity (equation 3.11).

3.4 Time Scale Constraint for Low-Reynolds-Number Model

It will be shown in chapter 5 that the computations carried out with the realizable $\overline{v^2}-f$ model are in good agreement with the experimental data. Thus, it is suggested to modify the original time scale in the low-Reynolds number $k-\varepsilon$ model (*AKN model*) to dampen the production of kinetic energy at the stagnation point. In section 3.1 was defined the eddy-viscosity for the *AKN model*. If that definition (equation 3.3) is substituted in the derivation of the realizability constraint (equations 3.17 and 3.18), the following time scale limit arises

$$\mathcal{T} \leq \frac{\sqrt{2}}{3}\frac{1}{C_\mu f_\mu S} \tag{3.24}$$

Combining the old time scale ($\mathcal{T} = k/\varepsilon$) with the new limit and after adding a model constant, the time scale for the *AKN model* in impinging flow is given by

$$\mathcal{T} \;=\; \min\left(\frac{k}{\varepsilon}\;,\;\frac{0.6}{\sqrt{6}\,C_\mu f_\mu S}\right) \tag{3.25}$$

3.5 Limiter for P_k in Low-Reynolds-Number Model

The time scale constraints presented in the previous sections have a direct effect on the eddy-viscosity which is proportional to the product of a velocity scale (squared) and a time scale. Thus, the realizable condition for stagnation flow works well in lowering the production rate of k (equation 3.4) when the time scale decreases. Instead of restricting the time scale, it is proposed to apply a limiter directly on the production of kinetic energy itself. This can be carried out via a bound on P_k, which is expected to operate in the stagnation region. The (constant) limiter makes the production rate of k (equation 3.1) proportional to the dissipation rate (ε) and is stated as,

$$P_k \;=\; \min\left(\,2\,C_\mu f_\mu k\,\mathcal{T}\,S^2\;,\;a\,\varepsilon\right) \tag{3.26}$$

where the old time scale (k/ε) is used for all the equations of the *AKN* model as well as in the first part of equation 3.26. Impinging jet flow simulations were performed to tune the limiter a.

3.6 Turbulent heat flux

The model for the temperature-velocity fluctuations is also based on the Boussinesq assumption

$$\overline{u_j\theta} = -\frac{\nu_t}{Pr_t}\frac{\partial \Theta}{\partial x_j} \tag{3.27}$$

where Pr_t is the turbulent Prandtl number. Replacing equation 3.27 into 2.10, yields the modeled temperature equation

$$U_j\frac{\partial \Theta}{\partial x_j} = \frac{\partial}{\partial x_j}\left[\left(\frac{\nu}{Pr} + \frac{\nu_t}{Pr_t}\right)\frac{\partial \Theta}{\partial x_j}\right] \tag{3.28}$$

The *laminar* and *turbulent* Prandtl numbers are set to 0.72 and 0.89, respectively for all the simulations.

Chapter 4

Computational Approach

4.1 The Solver

CALC-BFC (Boundary Fitted Coordinates) by Davidson and Farhanieh [8] is a CFD code for computations of two or three-dimensional steady/-unsteady, laminar/turbulent recirculating flows. The discretization technique is based on the *Finite Volume Method* (FVM) depicted in [18] and the main characteristics of the code are the use of a non-orthogonal coordinate system, the pressure-correction SIMPLE (*Semi-Implicit Method for Pressure-Linked Equations*) algorithm and the co-located grid arrangement with Rhie and Chow interpolation. A segregated *Tri- Diagonal Matrix Solver* (TDMA) is employed to solved the discretized algebraic equations. Hybrid central/upwind differencing, the QUICK and the Van Leer schemes are available for the discretization of the convective terms. However, it was found out the Hybrid scheme to perform good enough for the simulations accomplished in this study.

4.2 Axisymmetry considerations

The general transport equation for a variable Φ ($\Phi = U, V, k, \varepsilon, etc$) in steady state can be written as

$$\frac{\partial}{\partial x_j}\left(\rho U_j \Phi\right) = \frac{\partial}{\partial x_j}\left(\Gamma_\Phi \frac{\partial \Phi}{\partial x_j}\right) + S_\Phi \tag{4.1}$$

where S_Φ denotes the source per unit volume of the variable Φ and Γ is the diffusion coefficient. After performing the discretization of each transport equation, the corresponding algebraic equations have the following form

$$a_P \Phi_P = \sum a_{nb}\Phi_{nb} + S_U \tag{4.2}$$

where the index nb denotes the neighboring nodes of node P and S_U is the source term. The coefficient at the node under consideration can be

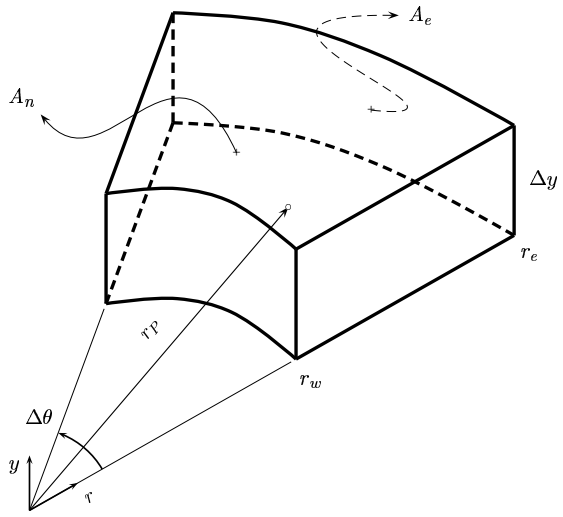

Figure 4.1: Modified control volume.

expressed (in two-dimensions) as

$$a_P = \sum a_{nb} - S_P = (a_E + a_W + a_N + a_S) - S_P$$

$$S = S_P \Phi_P + S_U$$

where E, W, N and S denote *east*, *west*, *north* and *south* respectively. Each coefficient contains the contribution due to convection and diffusion, and the general source term S which is split in a positive part (S_U) and negative part (S_P) holds the terms.

Regardless of the scheme used to discretize the convective terms, the area of each face of the control volume has to be corrected for the axisymmetric geometry of the impinging jet. For instance, the area of the east face A_e varies with the radial distance r and the area of the north face has to be computed according to cylindrical coordinates. These changes are better understood if a single finite volume is considered as in Figure 4.1. There is a clear correspondence between the cartesian coordinates (x, y, z) and the cylindrical ones (r, y, θ) which comes after correcting the areas of the east and north faces as follows [2]

$$A_e = (r_e \Delta\theta)\, \Delta y = (x_e \Delta z)\, \Delta y = x_e \left(A_e\right)^{old}$$

$$A_n = (r_P \Delta\theta)\, \Delta r = (x_P \Delta z)\, \Delta x = x_P \left(A_n\right)^{old}$$

$$r_P = \frac{1}{2}\left(r_w + r_e\right) = x_P$$

where r_P is the radial (x-direction) location of the control volume and the index old is used to designate the cartesian areas. Also, the volume needs to be corrected as

$$\delta V \;=\; (\delta V)^{old}\, r_P$$

The above changes ensure the right coefficients to be used in any of the algebraic equations given by 4.2.

4.3 Numerical Method

Diffusion terms were approximated using central differencing and hybrid central/upwind differencing or Van Leer was used for the discretization of convection in the momentum, temperature and turbulence equations. However, no appreciable difference in the calculated fields was observed when Van Leer scheme was used. Thus, hybrid central/upwind differencing was kept as the suitable scheme for convection. The dynamic and thermal fields are uncoupled in the impinging jet flow and therefore the thermal field was solved only once the dynamic field had converged. Under-relaxation factors ($0 \leq \alpha \leq 1$) were also used implicitly

$$\begin{aligned} a_P^{mod}\Phi_P^{new} &= \sum a_{nb}\Phi_{nb} + S_U^{mod} \\ a_P^{mod} &= \frac{a_P}{\alpha} \\ S_U^{mod} &= S_U + a_P^{mod}\,(1-\alpha)\,\Phi_P^{prev} \end{aligned}$$

Changes between successive iterations are slowed down using a suitable α in each discretized transport equation which stabilizes and improves the iterative process. Typical under-relaxation factors for the calculations carried out in this study are shown in Tables 4.1 and 4.2.

U	V	P	k	ε	Θ	ν_t
0.5	0.5	0.3	0.4	0.4	0.9	0.4

Table 4.1: Under-relaxation factors used with the low-Reynolds number model

U	V	P	k	ε	$\overline{v^2}$	f	Θ	ν_t
0.5	0.5	0.3	0.5	0.5	0.3	0.3	0.9	0.4

Table 4.2: Under-relaxation factors used with the $\overline{v^2} - f$ model

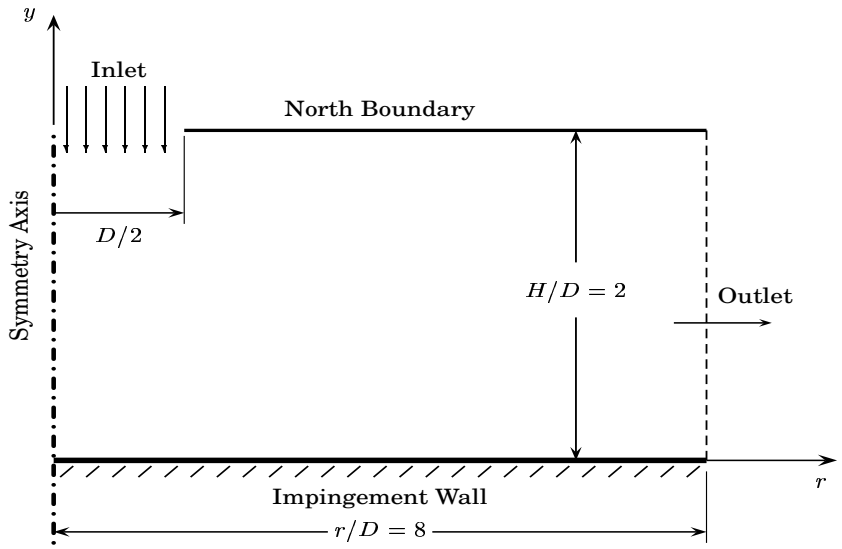

Figure 4.2: Flow domain.

It was also required to increase the number of sweeps to be performed by the TDMA solver for the pressure (P) and radial velocity (U) equations, to 30 and 5 sweeps respectively. This was executed in both models and faster convergence was observed. Convergence was reached when the total non-dimensionalized residuals for the momentum equations were below 10^{-4}. It was confirmed that reducing residuals below this value had no effect on results. Each residual is normalized by the total incoming flux of the dependent variable.

4.4 Domain and Boundary Conditions

Figure 4.2 is a sketch of the computational domain which shows a jet discharge height of 2 jet diameters and a domain extension of 8 jet diameters in the radial direction.

A fine, non-uniform structured grid of 145×121 nodes was used with a high resolution near the impingement wall and in the vicinity of the symmetry line where the jet evolves. A close-up of this region is shown in Figure 4.3. The clustered grid spacing at both size of $x/D = 0.5$ is required to fit the inlet boundary conditions coming from a fully--developed pipe flow. Different grid configurations were tested to ensure grid-independence, and the present grid was selected as the one which provides satisfactory results at a reasonable computational cost.

Figure 4.2 also outlines the boundary conditions employed in the impinging jet flow.

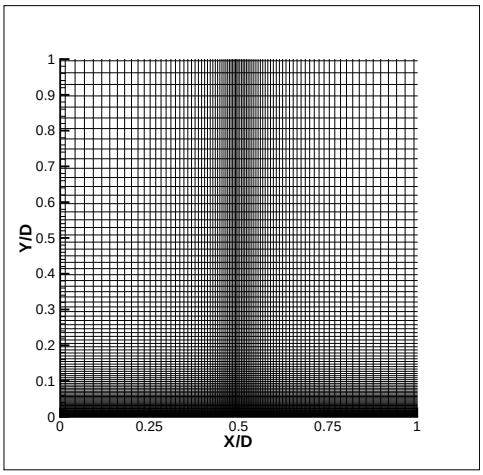

Figure 4.3: Focused view of the grid at the stagnation region.

Inlet Boundary

Fully-developed turbulent pipe flow with turbulent Reynolds number, $Re_\tau = 1286$ (based on the friction velocity and jet diameter) was computed separately to obtain the velocity and turbulent kinetic energy profiles as the inlet boundary conditions for each modeled assessed (Figure 4.4). Re_τ is chosen according to the pipe friction factor, so its value corresponds to the experimental Reynolds number of 23000 (based on the bulk velocity and jet diameter) for the jet simulations. In this computation, the grid spacing was chosen such that it perfectly fit the grid nodes at the inlet boundary of the impinging jet. The calculated profiles were normalized by the bulk velocity computed as

$$V_{bulk} = \frac{\int V dA}{A} \tag{4.3}$$

where A denotes the pipes cross sectional area.

When calculating the thermal field, the inlet temperature was fixed to a constant value ($T_{in} = 1$). Also, the radial velocity was set to zero ($U = 0$) and Neumann condition was prescribed for the remaining variables as

$$\left(\frac{\partial \Phi}{\partial y}\right)_{inlet} = 0 \tag{4.4}$$

where y is the axial direction (Figure 4.2) and Φ represents any of the variables different from the axial velocity (V) and turbulent kinetic energy (k) profiles already specified.

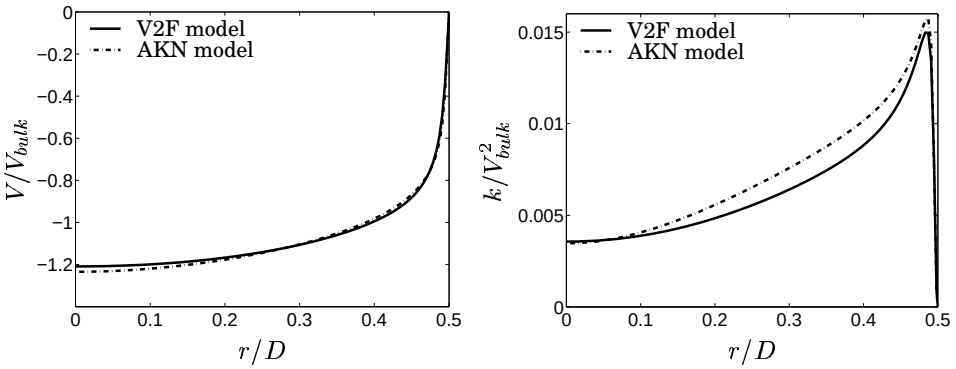

Figure 4.4: Inlet profiles.

Symmetry Axis

Along the axis of symmetry, zero-gradient (Neumann) condition was applied for the axial velocity component, turbulent scalars and temperature

$$\left(\frac{\partial \Phi}{\partial r}\right)_{symmetry} = 0 \tag{4.5}$$

To implement Neumann condition, the nodal value on the boundary of the domain was set equal to the neighboring nodal value inside the domain. The radial velocity was set to zero at this boundary $U = 0$, so there is no momentum flux across the symmetry line.

North Boundary

Slip condition was applied along this boundary. To implement this condition, the axial velocity was set to zero $V = 0$. Neumman condition was implemented for the radial velocity component (U), turbulent scalars and temperature

$$\left(\frac{\partial \Phi}{\partial y}\right)_{north} = 0 \tag{4.6}$$

Outlet

At the right hand outlet boundary, zero gradient conditions were applied to all the variables

$$\left(\frac{\partial \Phi}{\partial r}\right)_{outlet} = 0 \tag{4.7}$$

Although the flow through this boundary should be leaving the domain, during the iteration process flow is allowed to enter or exit through the boundary. Then, the velocity along this boundary is corrected in order to satisfy global continuity.

Impingement Wall

The wall boundary conditions for the turbulence quantities were already discussed in Chapter 3 for each model considered in this study. However, nothing was said concerning their implementation.

The boundary condition for the dissipation rate (ε) is implemented implicitly via its source term S_U (equation 4.2), while the value at the wall ($y = 0$) for the remaining turbulence quantities was explicitly assigned to the nodes lying on this boundary.

Constant heat flux was applied along the wall and it was implemented via the source term S_U for the discretized temperature equation. Besides, the south coefficient a_S is set to zero, so that no other means of heat flux takes place.

Chapter 5

Results and Discussion

5.1 Performance of the Time Scale Constraint

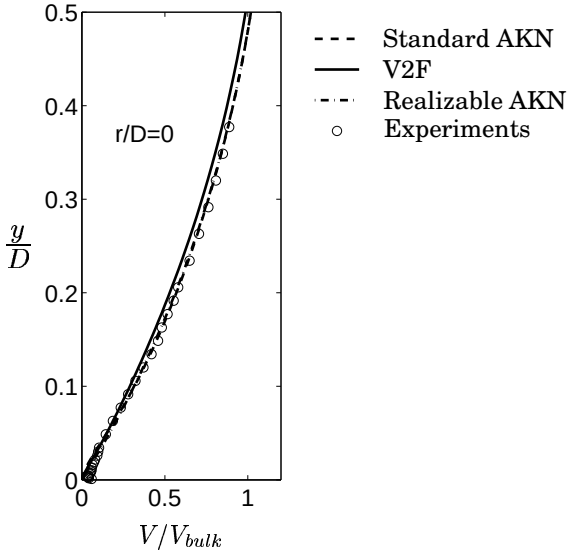

Figure 5.1: Velocity at the stagnation line normalized by the bulk velocity of the jet.

The performance of the *realizable V2F*, the *standard AKN* and *realizable AKN* models is considered in this section. The axial velocity on the stagnation line is given in Figure 5.1 showing that there is very little difference between the three predictions (in fact, the standard and realizable AKN models give almost the same results) and quite a good agreement with the experimental data is noted.

Also, a comparison of the measured velocity magnitude and the computations with the V2F model and the two versions of the AKN model at six different radial locations is presented in Figure 5.2. At $r/D = 0.5$, the three models predict slightly higher velocities. However, if one moves downstream and enters into the wall-jet region at $r/D = 1.0$,

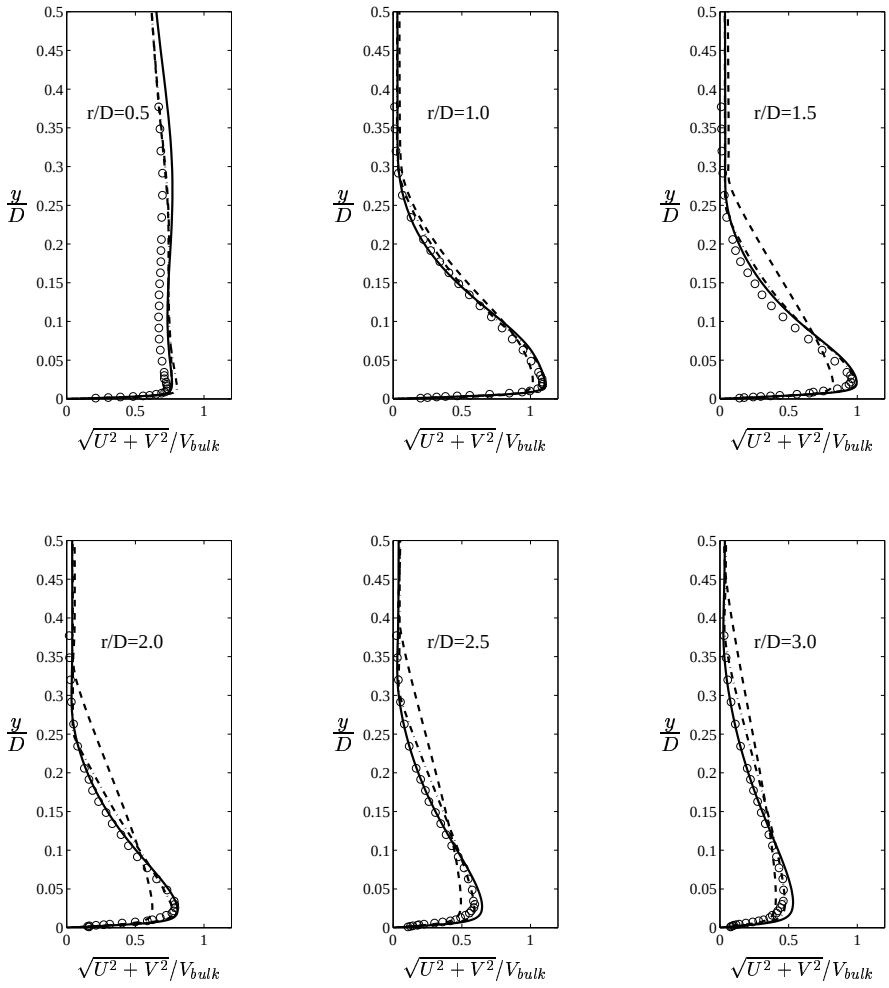

Figure 5.2: Profiles of the normalized velocity magnitude at different radial locations. Key as Figure 5.1.

the velocity magnitude increases from a value of zero to some maximum and subsequently decays to a very small value. The V2F and the realizable AKN models correctly predict the flow acceleration; there is excellent agreement with the data at this location. The standard AKN model predicts slightly lower velocities in the wall region and higher velocities in the outer region. Farther downstream, it can be noticed a better match between the V2F and the realizable AKN models with the experimental data. The standard AKN model carries on predicting lower velocities near the wall and higher velocities in the outer region, all the way downstream. As can be seen, the realizable AKN model performs much better than the standard AKN model when considering the velocity profiles.

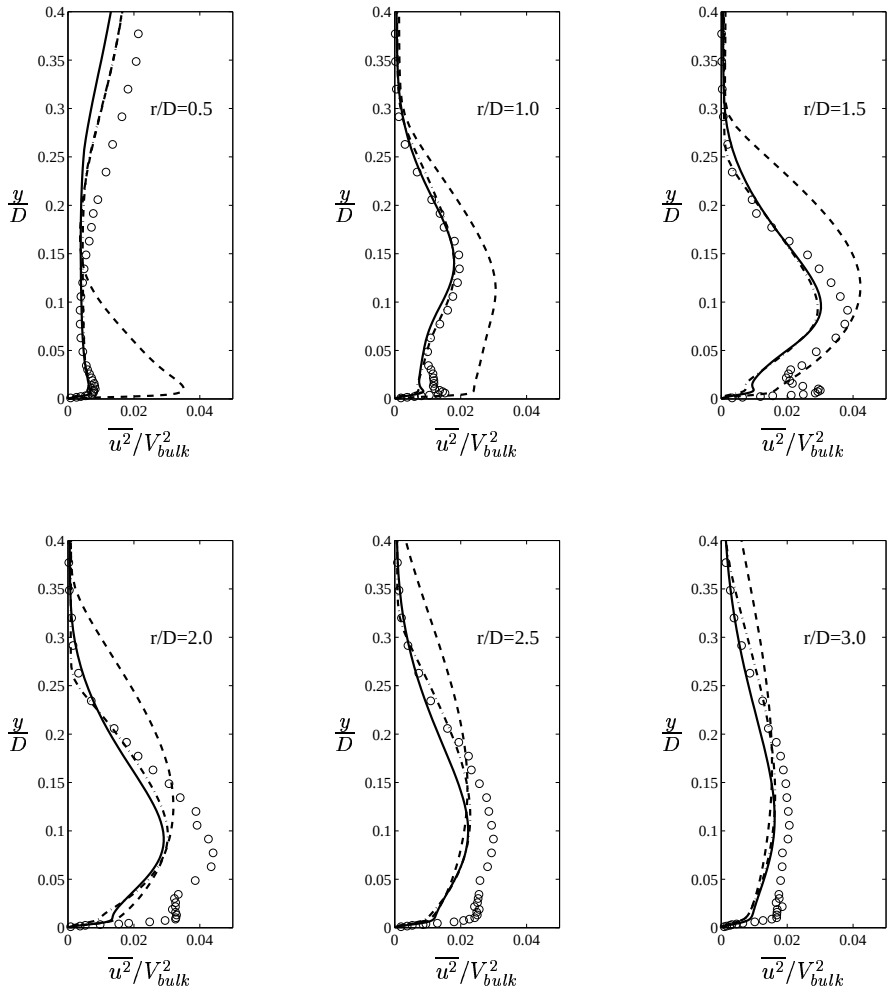

Figure 5.3: Normalized wall-parallel Reynolds stress profiles at different radial locations. Key as Figure 5.1.

The development of the Reynolds stresses as the flow develops away from the stagnation point is presented in Figures 5.3 to 5.5. Looking at the wall-parallel Reynolds stress profiles of Figure 5.3, it can be said that none of the models perfectly matches the experimental data. Nevertheless, the predicted profiles at $r/D = 0.5$ and $r/D = 1.0$ given by the V2F and realizable AKN models are reasonably good, especially in the wall region. On the other hand, the standard AKN model predicts too high $\overline{u^2}$ values at these two particular locations. The V2F gives quite good results even though the Boussinesq assumption (equation 2.11) is employed to compute this stress and again, very little difference is observed between the profiles given by the V2F and the realizable AKN models.

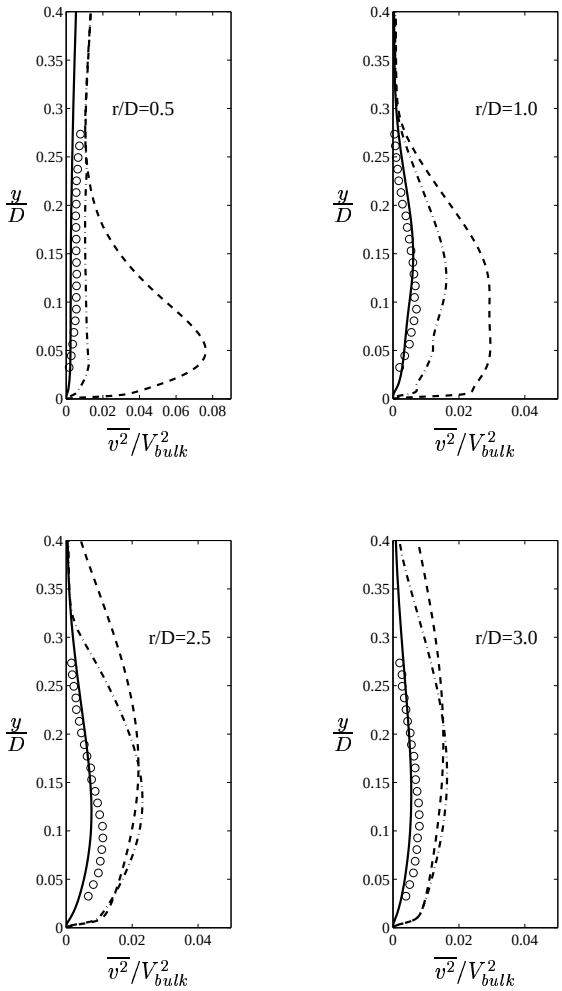

Figure 5.4: Normalized wall-normal Reynolds stress profiles at different radial locations. Key as Figure 5.1.

The differences between the models are more appreciable when looking at the wall-normal stress profiles of Figure 5.4. It is evident that the performance of the V2F model is outstanding compared to both versions of the AKN model. The main reason is due to the implementation of a $\overline{v^2}$ transport equation in the V2F model instead of using the Boussinesq assumption. However, it should be noticed the improved prediction obtained by the realizable AKN not too far from the stagnation line (at $r/D = 0.5$ and $r/D = 1.0$). It can be noticed that the V2F model yields a moderate anisotropy between the wall-parallel stress component seen in Figure 5.3 and the wall-normal component, especially for the first two profiles. Once again, the results given by the standard AKN model considerably deviate from the measured data.

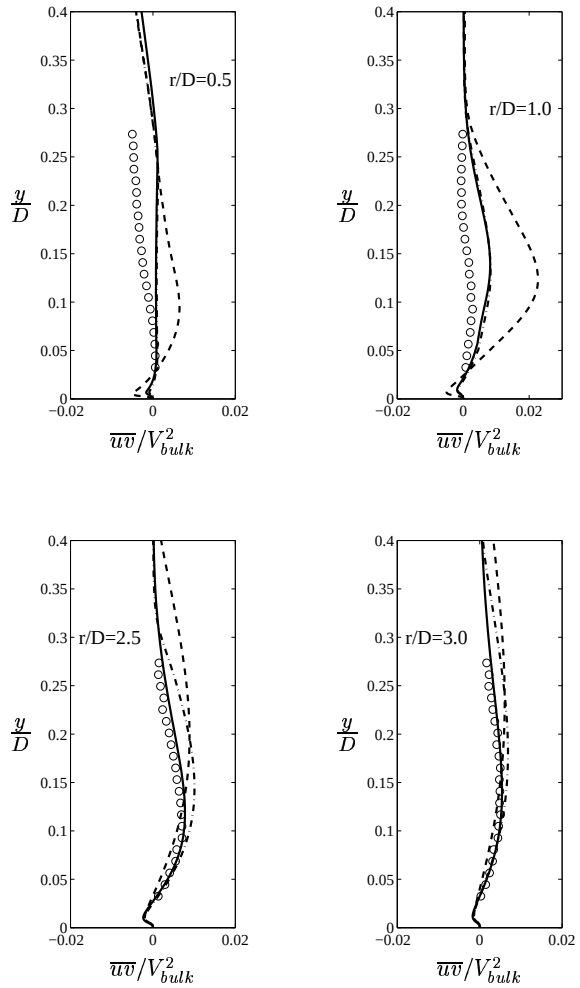

Figure 5.5: Normalized turbulent shear stress profiles at different radial locations. Key as Figure 5.1.

A similar behavior can be observed from the turbulent shear stress profiles of Figure 5.5. Again, the V2F and realizable AKN models give the most accurate account of the development, with the standard AKN model being less successful in matching the experimental data, though not as spectacularly so as for $\overline{v^2}$.

Measurements of the wall-normal Reynolds stress at the symmetry (stagnation) line are compared in Figure 5.6 with $2/3\,k$ from the two versions of the AKN model and the V2F model calculations, as well as $\overline{v^2}$ from V2F computations. This figure clearly shows that k predictions in the vicinity of the stagnation point obtained from the standard AKN model are one order of magnitude higher than $\overline{v^2}$, hence this model exceedingly over-estimates the fluctuating quantities and heat transfer

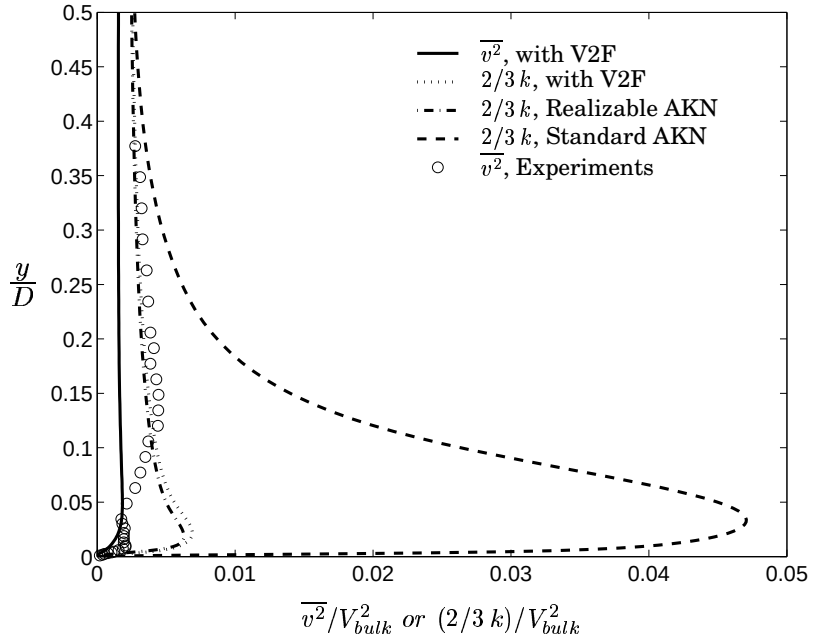

Figure 5.6: Normalized wall-normal Reynolds stress and turbulent kinetic energy on the stagnation line.

rates. On the other hand, a significant lower level of k is predicted by the realizable AKN, very similar to the result given by the V2F model. This is due to the time scale constraint which is expected to act in the stagnation region damping the production rate of kinetic energy.

Finally, some contours of the velocity field, the dissipation rate and turbulent kinetic energy are plotted in Figure 5.7. This figure is a composite: on the left half are contours of each variable predicted by the standard AKN and on the right predictions of V2F. The predicted velocity fields by both models (subfigures a and b) look quite similar to each other. However, ε and k contours (subfigures c and d) greatly differ from one model to the other. Focusing on the kinetic energy contours, it is observed a marked maximum near the wall on the symmetry axis, according to the standard AKN computations. This is responsible for the excessive heat transfer rate at the stagnation point, leading to an over-predicted Nusselt number as it will be shown later. The maximum value of k predicted by the standard AKN model is 55% higher than that by V2F. The location of this maximum is at about $r/D \approx 1.9$ for the V2F which has been confirmed by experimental work [4]. The increase in the turbulent energy away from the stagnation point is produced by high near-wall shear strains (region of strong streamline curvature) which generates turbulence energy. In addition, the shear layer reaches the wall in this region, carrying high levels of turbulence energy.

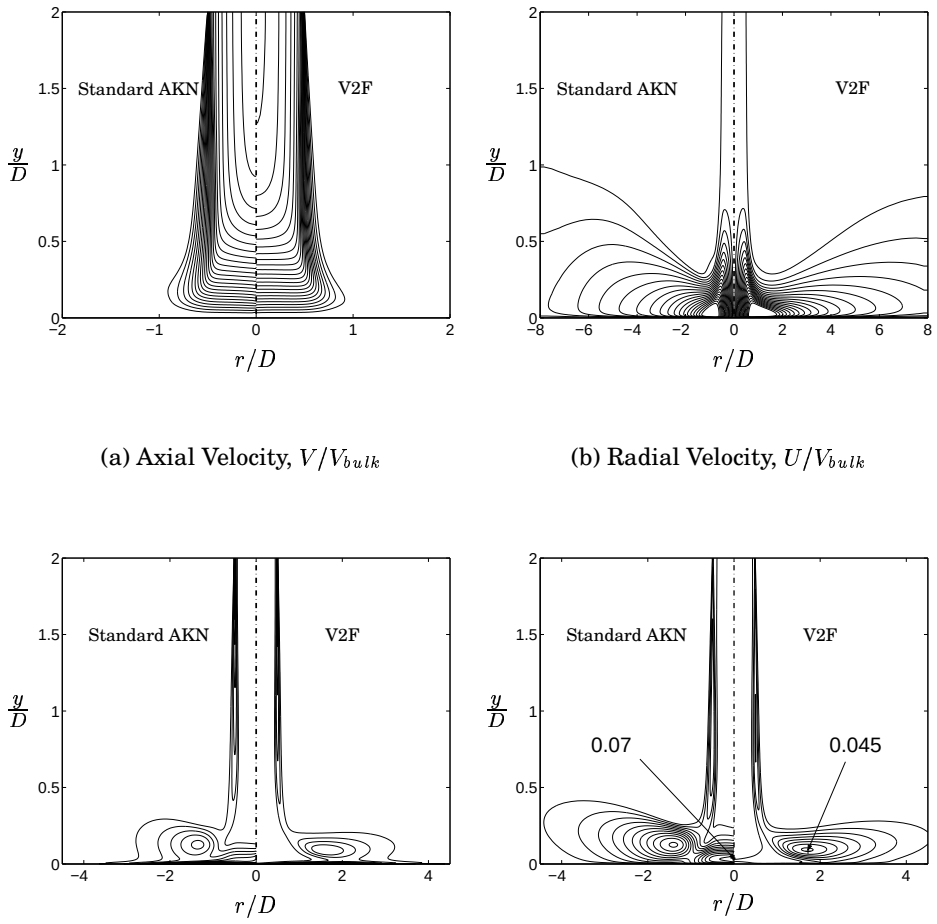

(a) Axial Velocity, V/V_{bulk}

(b) Radial Velocity, U/V_{bulk}

(c) Dissipation rate, $\varepsilon/\left(V_{bulk}^4/\nu\right)$

(d) Turbulent Kinetic Energy, k/V_{bulk}^2

Figure 5.7: Comparison of various contours obtained from two different turbulence models.

5.2 Limiter effect on the AKN model

Here is described how the limiter a in equation 3.26 was optimized. Several simulations were carried out for different values of a, ranging from 1.5 to 15 and the results were compared with the existing calculations obtained from the standard and realizable AKN models. The results presented below correspond to the most distinctive limiters found in this study, that is to say $a = 2.5,\ 5$ and 10.

The axial velocity on the symmetry line shown in Figure 5.8 indicates no limiter dependence as there is no perceptible difference between the three predictions, as well as very good agreement with the measured data is noticed. However, the predicted velocity profiles down-

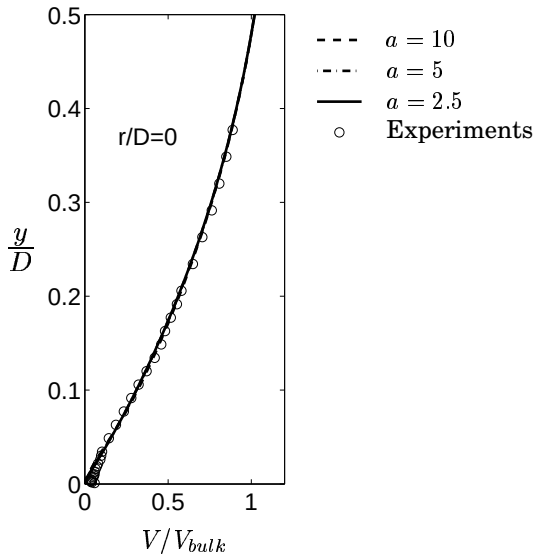

Figure 5.8: Normalized velocity at the stagnation line using three different limiters for P_k in the AKN model.

stream the stagnation line differ from each limiter, as it is shown in Figure 5.9. For example, at $r/D = 1.5$ in the wall-jet region the limiter $a = 2.5$ gives a more accurate prediction close to the wall than the other two limiters. Unfortunately, none of the limiters satisfactorily matches the experimental data as one moves away from the surface in the wall--jet region.

The limiters response is clearly differentiated when looking at the predicted turbulent kinetic energy on the stagnation line. k predictions from the AKN model setting $a = 10$ and $a = 5$ are still too high near the stagnation point, though much smaller than the value given by the standard AKN model. The prediction after adjusting a to 2.5 surprisingly gives as acceptable levels of k as the realizable version. Indeed, the two curves are fairly similar along the symmetry line. Thus, the limiter $a = 2.5$ was chosen as the suitable value to reduce the production rate of kinetic energy in the AKN model. It is important to emphasize that the limiter was not found by chance, but performing a set of simulations to tune its value.

5.3 Comparison of the results given by the Constraint and the Limiter

The results obtained from the AKN model employing the limiter $a = 2.5$ are compared to those given by the realizable and standard AKN models. Figures 5.11 and 5.12 show velocity profiles at different radial locations as it was shown in the previous sections. Again, a very good

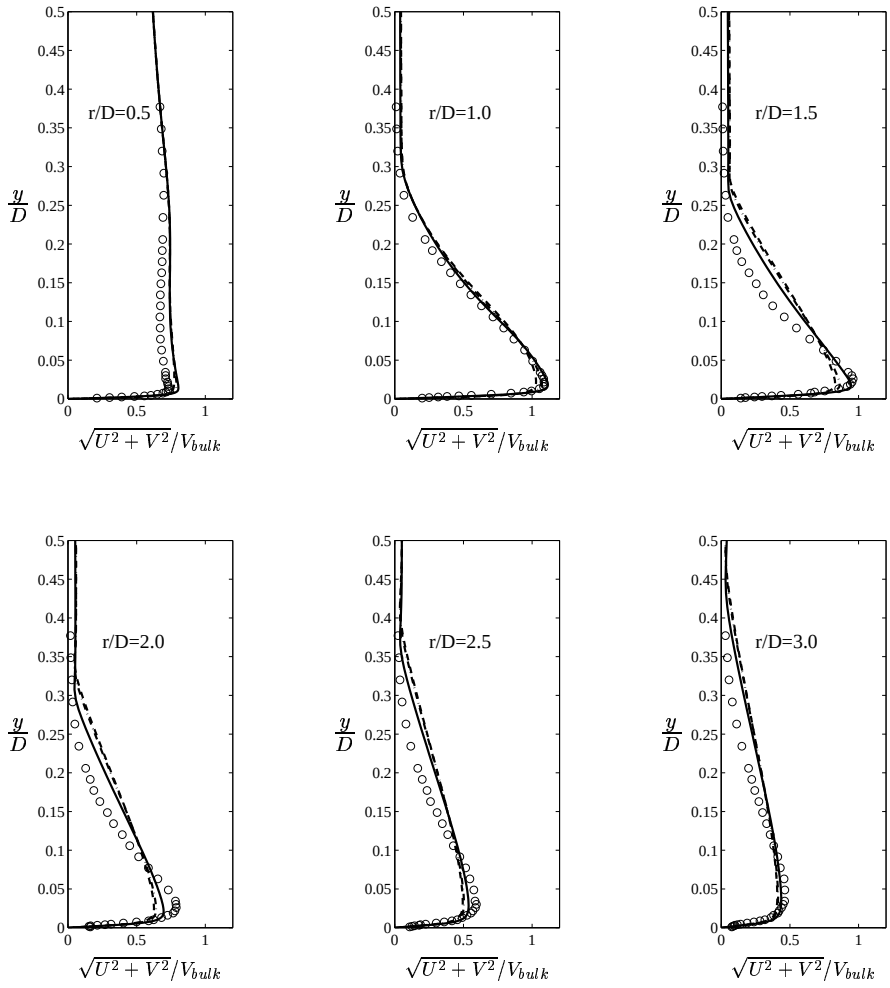

Figure 5.9: Limiter effect on velocity profiles, AKN model. Key as Figure 5.8.

agreement with the measured data is observed on the stagnation line for all the AKN versions. Downstream is noted the remarkable performance of the realizable version in predicting the velocity profiles, even though the limiter also improves the predictions compared to the results given by the standard AKN version. The development of the Reynolds stresses as the flow develops away from the stagnation point is presented in Figures 5.13 to 5.15. When looking at the three different sets of stress profiles, it can be noticed the predicted results given by the limiter are in between those given by the realizable and standard models. As it was expected, the realizable and limiter AKN models provide much better results in the stagnation region than those of the standard AKN model. Besides, far from the stagnation point (at $r/D = 3.0$) the results given by the three AKN versions differ very little, which means

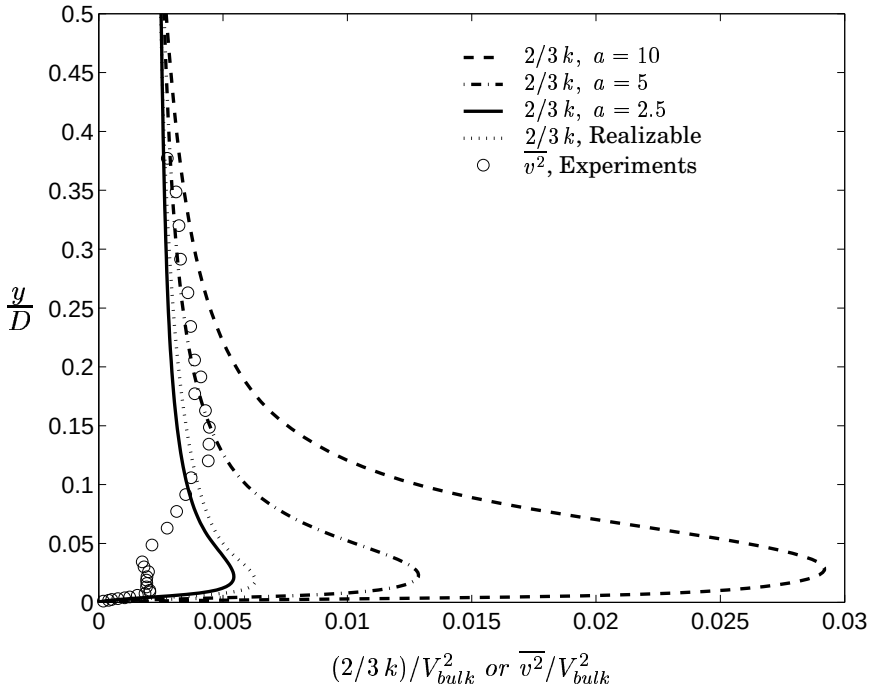

Figure 5.10: Limiter effect on the stagnation line, AKN model.

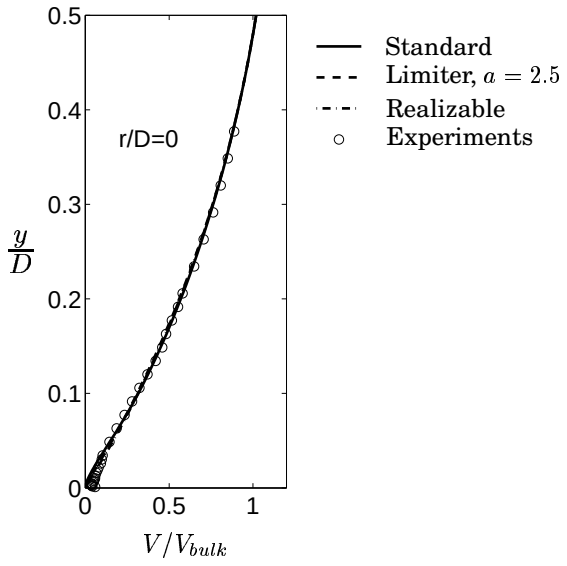

Figure 5.11: Normalized velocity at the stagnation line predicted by three versions of the AKN model.

a weak influence from the upstream conditions.

In addition, a comparison of the turbulent kinetic energy contours is shown in Figure 5.16. It is well noted the resemblance of the contours given by the realizable condition and the limiter. Also, the maximum occurs away from the stagnation line; both predicted values differ only

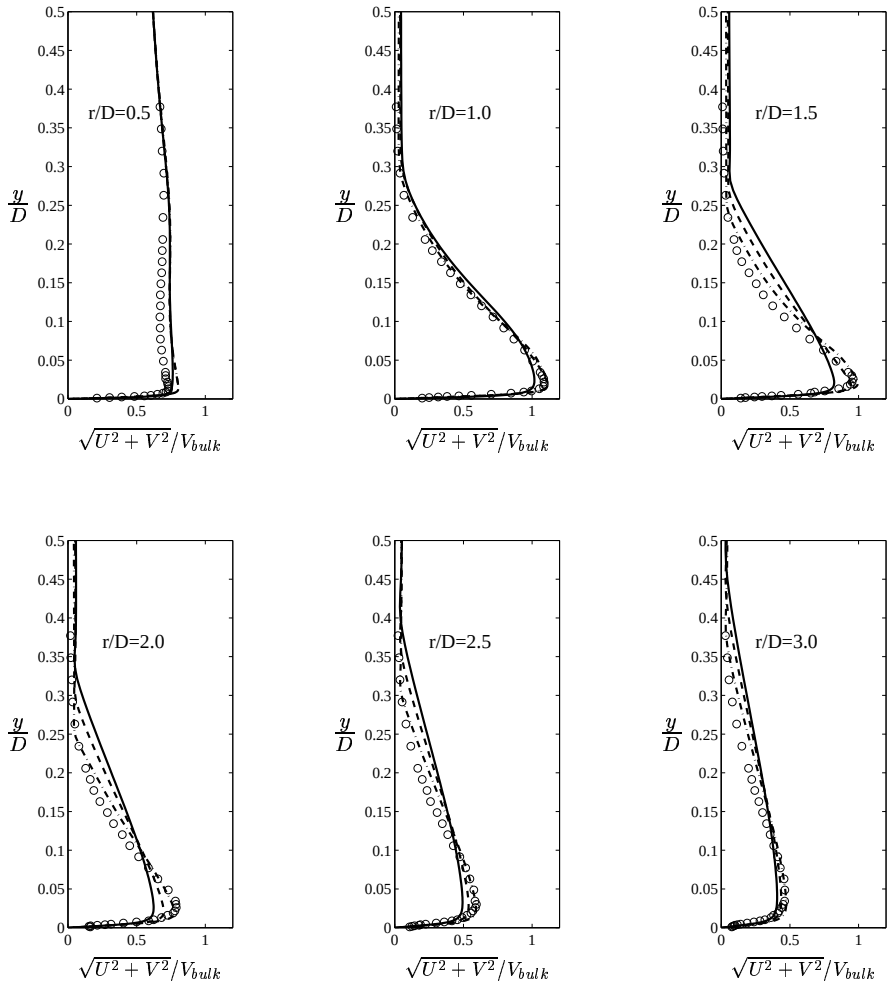

Figure 5.12: Predicted velocity profiles at different radial locations by three versions of the AKN model. Key as Figure 5.11.

slightly and take place approximately at the same location ($r/D \approx 1.9$). The results presented above indicate the similarity between the realizability constraint and the use of a limiter for the production rate of kinetic energy in the AKN model. Although the realizable AKN performs slightly better in predicting the Reynolds stress, it can be affirmed with no doubt that both approaches considerably improve the predictions given by the standard AKN.

5.3.1 Near-wall behavior

Here is analyzed the behavior of the strains in the vicinity of the wall. It is expected that the irrotational strains dominate in the stagnation region as the flow decelerates in the axial direction before turning at the

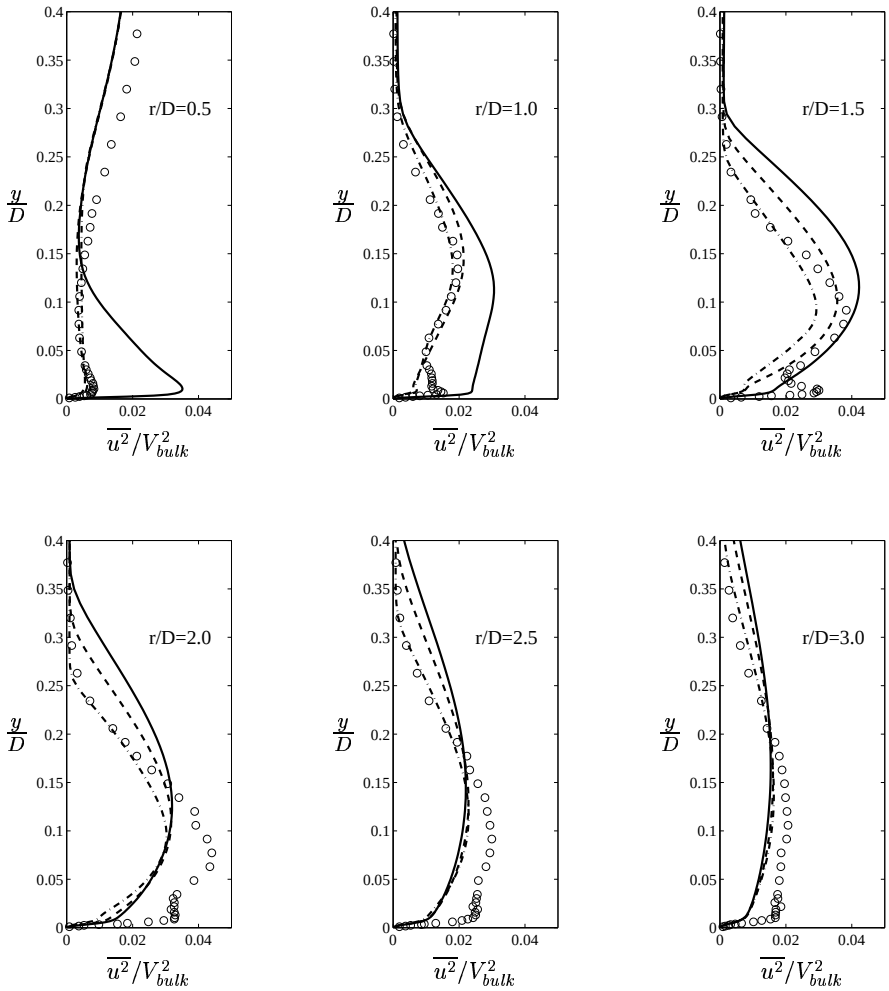

Figure 5.13: Predicted wall-parallel Reynolds stress profiles at different radial locations by three versions of the AKN model. Key as Figure 5.11.

wall. So, the normal strain $\partial V/\partial y$ represents an important contribution when calculating the wall-normal stress

$$\overline{v^2} \quad = \quad \frac{2}{3}k - 2\nu_t \frac{\partial V}{\partial y} \tag{5.1}$$

This is verified looking at the results given by the three versions of the AKN model in the stagnation region seen in Figure 5.17. $2/3\,k$ is also plotted for comparison. The normal strain has a negative value due to the flow deceleration in the proximity of the wall, which increases the wall-normal stress of equation 5.1. The three AKN versions point out the same trend to a more or less extent.

The opposite behavior is observed when looking at the results in the wall-jet region of Figure 5.18. Far from the stagnation point, the flow

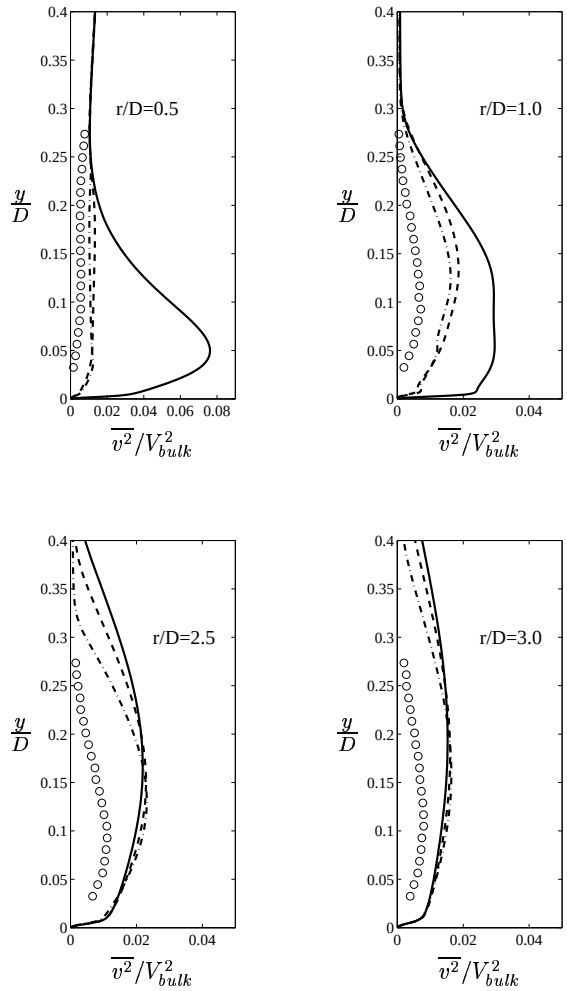

Figure 5.14: Predicted wall-normal Reynolds stress profiles at different radial locations by three versions of the AKN model. Key as Figure 5.11.

develops as a boundary layer flow dominated by the shear strains

$$\overline{uv} \quad = \quad -\nu_t \left(\frac{\partial U}{\partial y} + \frac{\partial V}{\partial r} \right) \tag{5.2}$$

Now the strain $\partial U/\partial y$ becomes important. As can be also seen, the normal strain $\partial V/\partial y$ goes to zero in the wall-jet region. This trend is accurately predicted by all versions of the AKN model. Thus, shear replaces normal straining as the principal energy generation mechanism.

5.3.2 Time-Scale Constraint and Limiter operation

The use of the different time-scales and the limiter ($a = 2.5$) in the domain are shown in Figure 5.19 for both AKN versions. For comparison,

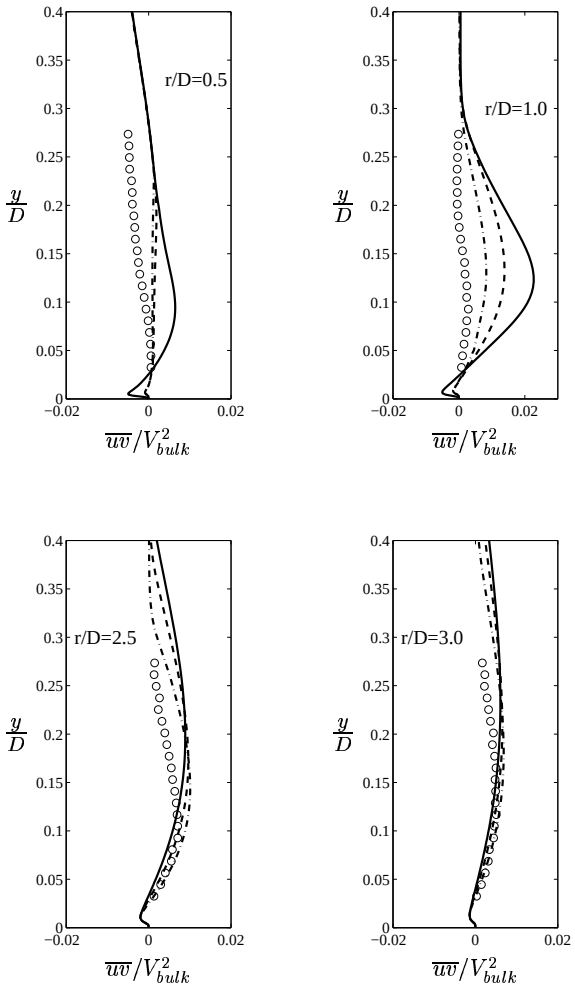

Figure 5.15: Predicted turbulent shear stress profiles at different radial locations by three versions of the AKN model. Key as Figure 5.11.

the time-scale usage of the V2F model is also presented.

There are many interesting features to point out. First, the time--scale constraint for the AKN and V2F models are active in the stagnation region as expected. However, there is also a narrow shaded area (sub-figure a) which starts at the inlet and goes down along the free jet region, where the time-scale constraint for the realizable AKN model is active. This was not expected to happen as the time-scale constraint should be active only in the stagnation region. This spurious behavior might be attributed to a high strain-rate magnitude S along the jet shear layer, which causes the time-scale constraint in equation 3.25 to be active. Nonetheless this does not greatly affect the predicted flow field.

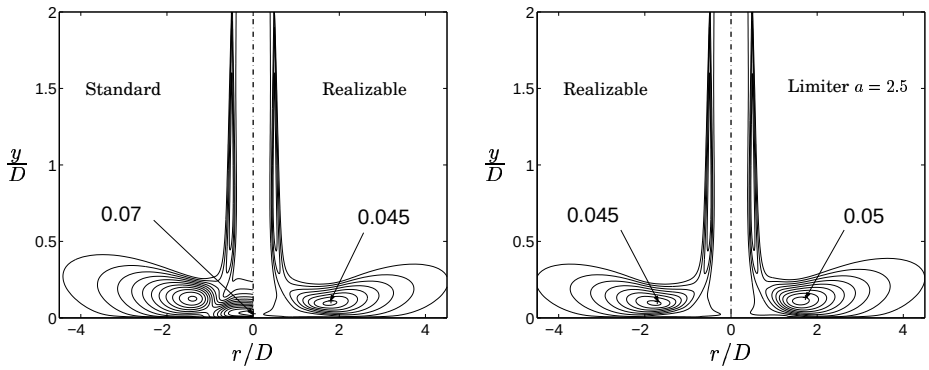

Figure 5.16: Comparison of turbulent kinetic energy contours obtained from three versions of the AKN model.

On the other hand, the limiter $a = 2.5$ only works at the stagnation region as it is depicted in sub-figure b. In fact, the shaded area where the limiter is used in the domain resembles a lot to that where the V2F time-scale constraint acts to lower the production rate of k (sub-figure c).

Also, the V2F highlights the use of the Kolmogorov limiter in equation 3.20 which is used in the near-wall region as well as close to the jet inlet, along a short and narrow area which is due to the convected pipe flow.

5.4 Heat transfer coefficient

If $T_{wall} \neq T_{in}$, convection heat transfer occurs in both the stagnation and wall-jet region. The Nusselt number in the impinging jet flow is evaluated as

$$Nu = \frac{h\,D}{\kappa} = \frac{(q_{wall}/C_p)\;D\,Pr}{\mu\;(T_{wall} - T_{in})} \tag{5.3}$$

where the ratio of the constant heat flux q_{wall} to the specific heat C_p is prescribed to calculate the Nusselt number, as the discretized equation of temperature is already normalized by C_p in the code. The wall temperature is estimated as

$$T_{wall} = T_1 + y_1\,(q_{wall}/C_p)\,\frac{Pr}{\mu} \tag{5.4}$$

where the index 1 denotes the nearest grid point from wall surface.

The predicted Nusselt number along the wall by the different turbulence models is shown in Figure 5.20. None of the models perfectly matches the experimental data, however big differences are observed

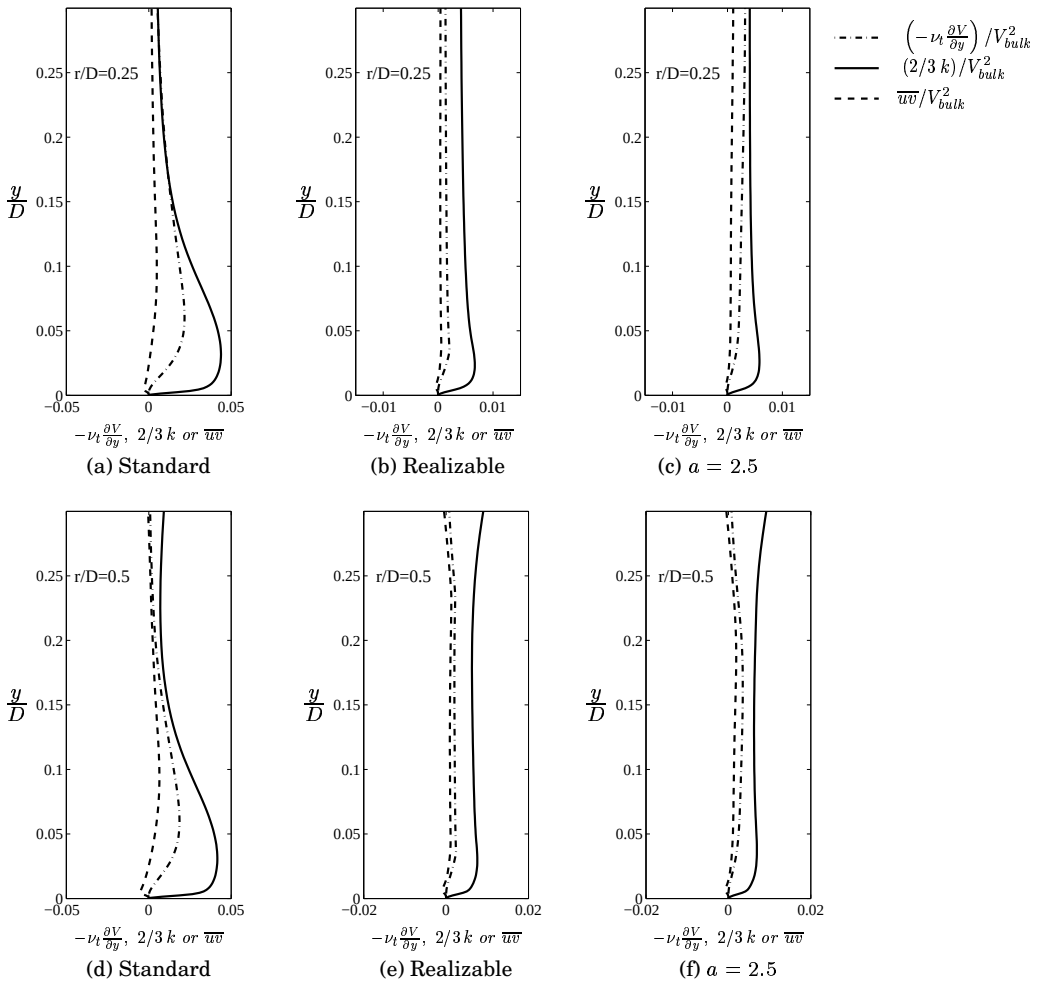

(a) Standard (b) Realizable (c) $a = 2.5$

(d) Standard (e) Realizable (f) $a = 2.5$

Figure 5.17: Influence of the strain-rates in the stagnation region. Results given by three versions of the AKN model.

to one another. The heat transfer rate is greatest at the stagnation point, with Nu at its maximum. Nevertheless, Nu is significantly over-predicted by the standard AKN model. In this model, the stagnation Nusselt number is about 41% higher than the measured value, whereas the V2F model prediction is only 3% too high. This high predicted value given by the standard AKN model is due to the spurious kinetic energy maximum at the stagnation point illustrated in Figures 5.6 and 5.7.

On the other hand, the realizable AKN and the limiter under-predict the Nusselt number at the stagnation point by 8.4% and 15% respectively. Again, it should be noted the resemblance in the predicted Nusselt number given by these two AKN versions.

Downstream of the stagnation region the standard AKN Nusselt number rapidly decreases and approaches the predicted values of the other two AKN versions. For $r/D \geq 1.5$ all the models, including the

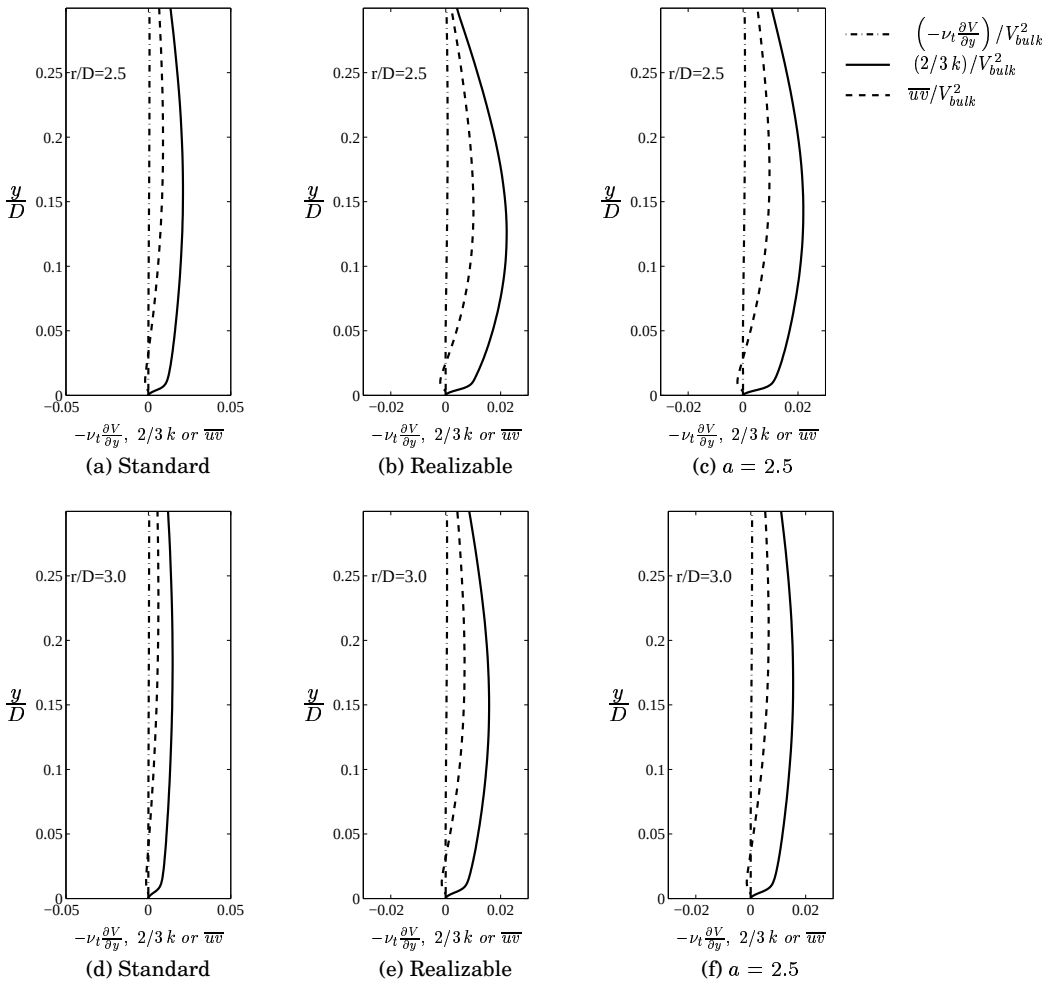

(a) Standard (b) Realizable (c) $a = 2.5$

(d) Standard (e) Realizable (f) $a = 2.5$

Figure 5.18: Influence of the strain-rates in the wall-jet region. Results given by three versions of the AKN model.

V2F, under-predict the experimental results. The secondary peak in Nusselt number, observed in the experiments of reference [3] at $r/D \approx 2$, is probably caused by an increase in the turbulent kinetic energy away from the stagnation region, near the point where the shear layer is impinging on the wall. However, none of the present models predict this local rise in Nu.

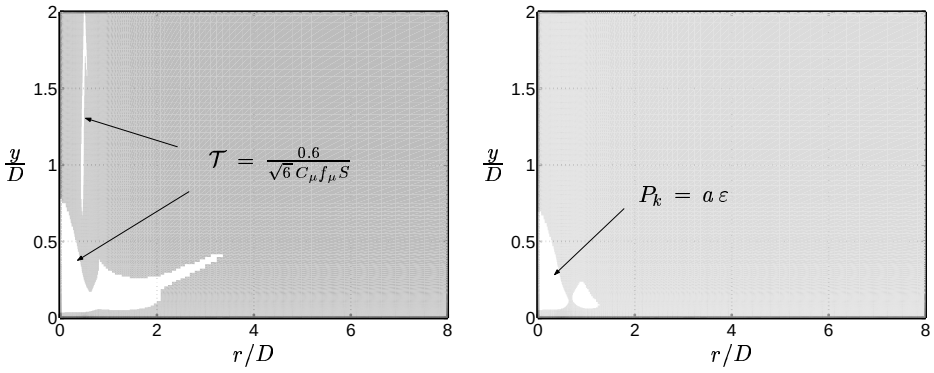

(a) Realizable AKN model

(b) Limiter $a = 2.5$, AKN model

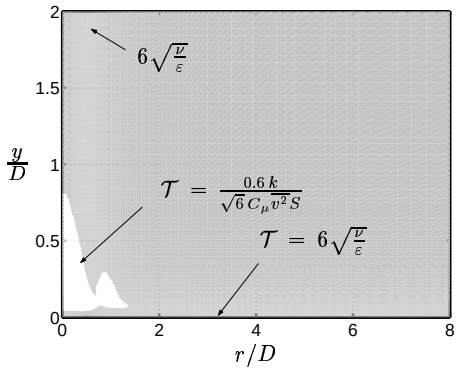

(c) V2F model

Figure 5.19: Regions where constraints are active (colored white).

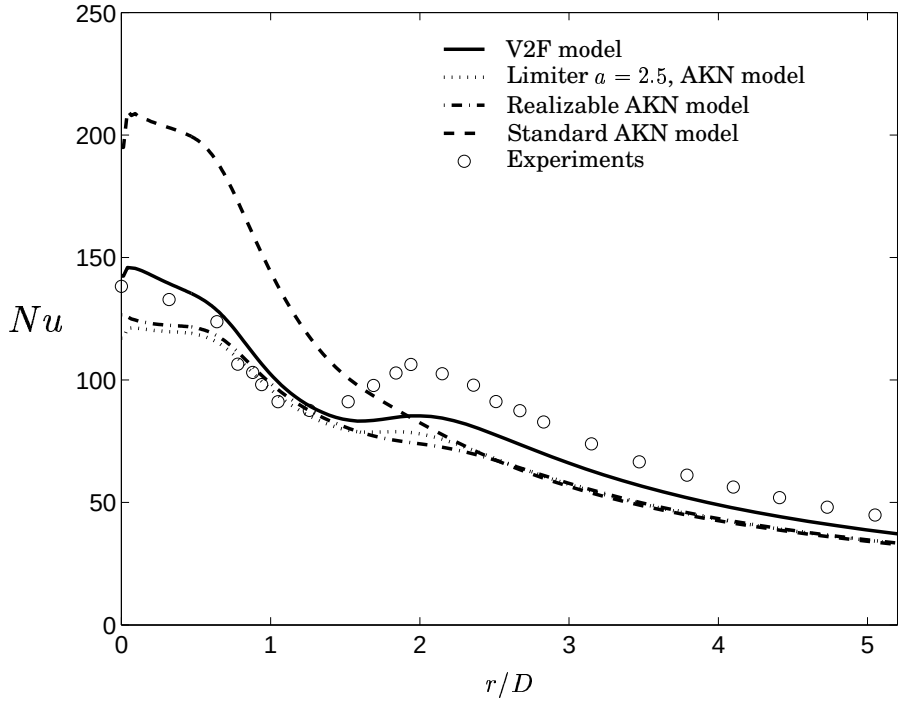

Figure 5.20: Variation of Nusselt number with radius.

Chapter 6

Future Work

All the previous computations have been conducted at a Reynolds number of 2.3×10^4. Although the realizable and limiter forms of the AKN model give satisfactory flow results, it is essential to check their accuracy at different Re_D. So, simulations should be carried out to validate the time-scale constraint and the limiter as compulsory variations of the AKN model when dealing with stagnation flow regimes. It would be interesting to find out whether the limiter $a = 2.5$ can be considered a fixed value or not. Also, the effect of the Reynolds number on the Nusselt number should be considered.

Furthermore, the effect of varying the jet distance H/D needs to be evaluated. However, it is required to look for a wider range of experimental data in order to compare the calculated results for the various impinging jet configurations and flow conditions.

A non-linear $\overline{v^2} - f$ model has been recently proposed to take into account the stress anisotropy when calculating heat transfer. So, improved heat transfer predictions might be obtained by solving the temperature equation based on the flow field already calculated by the current linear realizable $\overline{v^2} - f$ model. Hopefully this model will be able to predict the correct shape of the Nusselt number profile.

Bibliography

[1] K. Abe, T. Kondoh, and Y. Nagano. A new turbulence model for predicting fluid flow and heat transfer in separating and reattaching flows - 1. Flow field calculations. *Int. J. Heat Mass Transfer*, 37:139–151, 1994.

[2] D. G. Barhaghi. DNS and LES of Turbulent Natural Convection Boundary Layer. Thesis for Licentiate of Engineering, Dept. of Thermo and Fluid Dynamics, Chalmers University of Technology, Gothenburg, 04/06, 2004.

[3] J. Baughn and S. Shimizu. Heat Transfer Measurements From a Surface With Uniform Heat Flux and an Impinging Jet. *Journal of Heat Transfer*, 111:1096–1098, 1989

[4] M. Behnia and S. Parneix and P.A. Durbin. Prediction of heat transfer in an axisymmetric turbulent jet impinging on a flat plate. *Int. J. Heat Mass Transfer*, 41:1845–1855, 1998.

[5] D. Cooper, D. Jackson, B. Launder and G. Liao. Impinging jet studies for turbulence model assessment–I. Flow-field experiments. *Int. J. Heat Mass Transfer*, 36:2675–2684, 1993.

[6] T. Craft, J. Graham, and B. Launder. Impinging jet studies for turbulence model assessment–II. An examination of the performance of four turbulence models. *Int. J. Heat Mass Transfer*, 36:2685–2697, 1993.

[7] L. Davidson. An introduction to turbulence models. Technical Report 97/2, Dept. of Thermo and Fluid Dynamics, Chalmers University of Technology, Gothenburg, 1997.

[8] L. Davidson and B. Farhanieh. CALC-BFC: A finite-volume code employing collocated variable arrangement and cartesian velocity components for computation of fluid flow and heat transfer in complex three-dimensional geometries. Rept. 95/11, Dept. of Thermo and Fluid Dynamics, Chalmers University of Technology, Gothenburg, 1995.

[9] L. Davidson and P.V. Nielsen and A. Sveningsson. Modifications of the v^2-f Model for Computing the Flow in a 3D Wall Jet. *Turbulence Heat and Mass Transfer 4*, begell house, inc. 577–584, New York, Wallingford (UK), 2003.

[10] R. Ding. Experimental Studies of Turbulent Mixing in Impinging Jets. Doctoral thesis, Div. of Fluid Mechanics, Dept. of Heat and Power Engineering, Lund Institute of Technology, Lund, Sweden, 2004.

[11] M. Dianat and M. Fairweather and W. Jones. Predictions of axisymmetric and two-dimensional impinging turbulent jets. *Int. J. Heat Fluid Flow*, 17(6):530–538, 1996.

[12] P.A. Durbin. Near-wall turbulence closure modeling without damping functions. *Theoretical and Computational Fluid Dynamics*, 3:1–13, 1991.

[13] P.A. Durbin. On the $k-3$ stagnation point anomaly. *Int. J. Heat Fluid Flow*, 17(1):89–90, 1995.

[14] S. Gant. Development and Application of a New Wall Function for Complex Turbulent Flows. PhD thesis, Thermodynamics and Fluid Mechanics Div., Dept. of Mechanical, Aerospace and Manufacturing Engineering, University of Manchester, Institute of Science and Technology, Manchester, UK, 2002.

[15] R. Jia. Turbulence Modelling and Parallel Solver Development Relevant for Investigation of Gas Turbine Cooling Processes. Doctoral thesis, Div. of Heat Transfer, Dept. of Heat and Power Engineering, Lund Institute of Technology, Lund, Sweden, 2004.

[16] F-S Lien and G. Kalitzin. Computations of transonic flow with the v^2-f turbulence model. *Int. J. Heat Fluid Flow*, 22(1):53–61, 2001.

[17] A. Sveningsson. private communication. Dept. of Thermo and Fluid Dynamics, Chalmers University of Technology, Gothenburg, Sweden, 2003.

[18] H.K. Versteegh and W. Malalasekera. *An Introduction to Computational Fluid Dynamics - The Finite Volume Method*. Longman Scientific & Technical, Harlow, England, 1995.